

UNIVERSITY OF CALIFORNIA, BERKELEY

BERKELEY • DAVIS • IRVINE • LOS ANGELES • RIVERSIDE • SAN DIEGO • SAN FRANCISCO



SANTA BARBARA • SANTA CRUZ

COLLEGE OF ENGINEERING
ELECTRONIC RESEARCH LABORATORY
253 CORY HALL
(510) 642-2301
<http://www.eecs.berkeley.edu/~erl>

BERKELEY, CA 94720-1774

Annual Progress Report submitted to the Naval Research Laboratory

**Simulation of Low Frequency Noise in a CCTWT
N00173-98-1-G001
May, 98 – March, 99**

**Professor Charles K. Birdsall
Principal Investigator**

**University of California, Berkeley
Electronics Research Laboratory**

| REPORT DOCUMENTATION PAGE | | | | <i>Form Approved</i> <i>OMB No. 0704-0188</i> | | |
|--|-------------|-----------------------------------|-------------------------------|---|---|--|
| Public reporting burden for this collection of information is estimated to average 1 hour per response, including the time for reviewing instructions, searching data sources, gathering and maintaining the data needed, and completing and reviewing the collection of information. Send comments regarding this burden estimate or any other aspect of this collection of information, including suggestions for reducing this burden to Washington Headquarters Service, Directorate for Information Operations and Reports, 1215 Jefferson Davis Highway, Suite 1204, Arlington, VA 22202-4302, and to the Office of Management and Budget, Paperwork Reduction Project (0704-0188) Washington, DC 20503. | | | | | | |
| PLEASE DO NOT RETURN YOUR FORM TO THE ABOVE ADDRESS. | | | | | | |
| 1. REPORT DATE (DD-MM-YYYY) 5/27/99 | | 2. REPORT DATE Annual Progress | | 3. DATES COVERED (From - To) 5/1/98 to 3/31/99 | | |
| 4. TITLE AND SUBTITLE Simulation of Low Frequency Noise in a CCTWT | | | | 5a. CONTRACT NUMBER N00173-98-1-G001 | | |
| | | | | 5b. GRANT NUMBER N00173-98-1-G001 | | |
| | | | | 5c. PROGRAM ELEMENT NUMBER | | |
| 6. AUTHOR(S) C.K. Birdsall J.P. Verboncoeur P.J. Christensen | | | | 5d. PROJECT NUMBER 68-4000-98 | | |
| | | | | 5e. TASK NUMBER | | |
| | | | | 5f. WORK UNIT NUMBER | | |
| 7. PERFORMING ORGANIZATION NAME(S) AND ADDRESS(ES) University of California, Berkeley Electronics Research Laboratory 253 Cory Hall Berkeley, CA 94720 | | | | 8. PERFORMING ORGANIZATION REPORT NUMBER 442427-25803 | | |
| 9. SPONSORING/MONITORING AGENCY NAME(S) AND ADDRESS(ES) Naval Research Laboratory Code 6841 4555 Overlook Avenue, SW Washington, DC 20376-5320 | | | | 10. SPONSOR/MONITOR'S ACRONYM(S) | | |
| | | | | 11. SPONSORING/MONITORING AGENCY REPORT NUMBER | | |
| 12. DISTRIBUTION AVAILABILITY STATEMENT Distribution unlimited | | | | | | |
| 13. SUPPLEMENTARY NOTES | | | | | | |
| 14. ABSTRACT <p style="margin: 0;">The report describes the progress made studying the low frequency noise in a coupled cavity traveling wave tube. Simulations using the particle-in-cell code, XOOPIC, indicate that plasma is generated by the ionization of a background gas. The plasma is trapped in the potential depression of the beam, which is formed in the radial direction of the beam, which is formed in the radial direction by the radial space charge field, and in the axial direction due to scalloping of the beam in the external solenoidal magnetic field. As the ion density exceeds the beam density, the ionization (plasma) electrons are observed to be expelled axially, followed in 20 ns by radial expulsion of the ions. The plasma then begins to build up again, and the oscillation repeats. The next step in the study is to include the microwave circuit in the simulation, to observe the impact of the oscillation on the output power. In addition, means of eliminating or controlling the oscillation will be studied.</p> | | | | | | |
| 15. SUBJECT TERMS noise, traveling wave tube, simulation, particle-in-cell, ions, plasma | | | | | | |
| 16. SECURITY CLASSIFICATION OF: | | | 17. LIMITATION OF ABSTRACT | 18. NUMBER OF PAGES | 19a. NAME OF RESPONSIBLE PERSON | |
| a. REPORT | b. ABSTRACT | c. THIS PAGE | | 55 | Charles Birdsall | |
| | | | | | 19b. TELEPHONE NUMBER (Include area code) 510-643-6631 | |

Simulation of Low Frequency Noise in a CCTWT

prepared by:

J. P. Verboncoeur, P. J. Christenson, and C. K. Birdsall
Plasma Theory and Simulation Group
Department of Electrical Engineering and Computer Science
University of California
Berkeley, CA 94720-1770
johnv@eecs.berkeley.edu

prepared for:

B. Levush
Naval Research Laboratory

May 1 1998 to Mar. 30 1999

19990607 025

DISTRIBUTION STATEMENT A
Approved for Public Release
Distribution Unlimited

CONTENTS

| | | |
|----------|--|-----------|
| 0 | Executive Summary | ii |
| 1 | Introduction | 1 |
| 1.1 | Scope | 1 |
| 1.2 | PTSG Members | 1 |
| 1.3 | Outline of Report | 2 |
| 2 | Background | 3 |
| 3 | Physical Model | 5 |
| 4 | Computational Model | 7 |
| 5 | Simulation Results | 13 |
| 5.1 | Beam in Vacuum | 13 |
| 5.2 | Grid Effects | 17 |
| 5.3 | Immobile Ion Lens | 21 |
| 5.4 | Self-Consistent Gun with H Gas | 31 |
| 5.4.1 | Plasma Buildup | 31 |
| 5.4.2 | Exodus Mechanisms | 36 |
| 5.4.3 | Phase Shift | 42 |
| 5.4.4 | Ionization Enhancement Coefficient | 44 |
| 5.4.5 | Energy and Angular Distributions Exiting the Gun | 44 |
| 6 | Conclusions | 48 |
| 6.1 | Future Work | 49 |
| 7 | Acknowledgments | 50 |
| A | Phase Calculation | 51 |

Approved for Public Release
Distribution Unlimited

0. EXECUTIVE SUMMARY

In the course of this reporting period, a number of models were successful in increasing our understanding of the low frequency noise in the CCTWT. Based on a number of proposed oscillation mechanisms, this study simulated the CCTWT using the self consistent XOOPIC particle-in-cell code [12]. XOOPIC can include the plasma either analytically or self consistently using a Monte Carlo collision model for the electron-neutral ionization process.

First, a simple PIC model of the gun and drift tube were constructed to provide a basic understanding of the device. The results demonstrated the scalloping of the beam, as well as the potential wells formed by the expansion and contraction of the space charge of the beam.

A study of the numerical effects of grid resolution and the stairstep approximation for the cathode demonstrated that these are within acceptable ranges for this parameter set.

Based on theoretical calculations of other researchers, a model was constructed to study the effects of an immobile ion lens in the anode-cathode gap. This model indicated that the ion lens was capable of overfocusing the beam and affecting the magnitude and spatial location of the potential wells. However, the model also indicated that ion densities considerably higher than the beam density are required to achieve these effects, and the perturbations are non-oscillatory, and therefore unlikely candidates for the source of the noise.

Finally, a self consistent PIC-MCC model which included electron impact ionization was performed on the gun and drift tube. This model demonstrated oscillations at the scaled pressure of 10 mTorr, which correlates to a CCTWT pressure of about 10 μ Torr. In addition, the plasma was observed to fill the scallops, and an oscillation of the plasma density resulted in oscillations of the potential above the anode potential. The ions were observed to leave radially, while the slow ionization electrons were observed to leave axially toward the collector. Once the plasma density dropped and the potential also decreased, the cycle began again with the plasma buildup. The beam is weakly perturbed by the oscillation of the potential, and the result can be seen in the velocity of the beam, leading to oscillations in the coupling with the circuit. The velocity phase space evidence supports the exodus mechanism as well, and the energy and angular distribution functions of the ionization electrons exiting the system include the signature of the oscillation.

1. INTRODUCTION

1.1. Scope

This report describes the progress made during the period from the start of the project through the first year ending March 31, 1999.

The Plasma Theory and Simulation Group (PTSG) is primarily involved in the simulation and theory of plasma and vacuum electronics devices. Here, we define plasma in a broad sense to include neutral and non-neutral plasmas, such as electron beams. The PTSG also develops, releases, and supports a number of plasma simulation codes. The codes are in use by hundreds of researchers, educators and students internationally. All PTSG codes are freely available via the Internet at <http://ptsg.eecs.berkeley.edu>.

1.2. PTSG Members

The Plasma Theory and Simulation Group at the University of California, Berkeley currently consists of one professor, one research engineer, two postdoctoral researchers, and five Ph.D. students, as well as a varying number of industrial and academic visitors. The PTSG members involved in this project during the research period included:

- Prof. C. K. Birdsall, principal investigator
- Dr. J. P. Verboncoeur, research engineer
- Dr. P. J. Christenson, postdoctoral researcher
- Dr. H. Smith, postdoctoral researcher
- K. C. Cartwright, graduate student researcher
- W.-G. Qiu, graduate student researcher

In addition, significant contribution has been made to this effort from collaborations with W. James (CPI), as well as many researchers from the Naval Research Laboratory, SAIC, Crane Naval Surface Warfare Center, and affiliated companies and consultants.

1.3. Outline of Report

In Section 2, the general ion noise problem is described, and research into ion noise is briefly summarized. In Section 3, the physical model is described, while in Section 4, the computational approximations and models used in the code are described. The results of the electron gun simulations are described in Section 5, including the vacuum beam, discrete grid effects, immobile ion lens, and fully self consistent electron gun with background gas. In Section 6, the conclusions are presented, along with plans for future work. The derivation of the phase change calculation is contained in Appendix A.

2. BACKGROUND

The CPI coupled cavity traveling wave tube (CCTWT), shown schematically in Fig. 2.1, is a key piece in a naval radar platform. In some large fraction of tubes, low frequency noise close to the carrier frequency limits the performance of the CCTWT. It operates in continuous wave (CW) mode at 20.5 kV, 2.8 A for 10 kW output power. The perveance is $0.95 \times 10^{-6} \text{ A/V}^{3/2}$. The beam propagates in near-confined flow, with a peak axial magnetic field of about 0.263 T, with beam scalloping of 5-10%. The cathode area convergence is 50:1. The mean beam radius is about 2 mm in the drift tube, and propagates through a series of coupled cavities with inner radius of about 3 mm. The circuit section is about 20 cm in length. The beam is collected at a depressed collector, with 97% transmission for $V_{dep} = 13 \text{ kV}$.

Sidebands are observed at low frequency, in the sub kHz range. The low frequency can be seen as sawtooth modulation of the output power signal, with a sawtooth period $5 < \tau < 20 \text{ msec}$. The sawtooth oscillations occur immediately when the CCTWT is turned on, and seem relatively insensitive to the gun voltage and current. Small changes in magnetic field of about 1% can affect the frequency of the sidebands. The shape and frequency of the sawtooth oscillations appears to depend upon the input power of the driving signal.

Similar low frequency oscillations have been observed in klystrons and TWTs by Clough et al. [1]. Clough attributed the low frequency oscillations to formation of a potential trap for ions generated by ionization of residual background gas. Oscillations observed in the kHz range by Klostermann et al. [4] were called "virtual anode oscillations".

A study of ion noise in a klystron tube was performed by Smith [9]. This klystron operated in the UHF band, with a 17.5 kV, 4.6 A beam. The magnetic field was 400 G, and the beam radius was 1 cm in a 1.25 cm radius drift tube. The

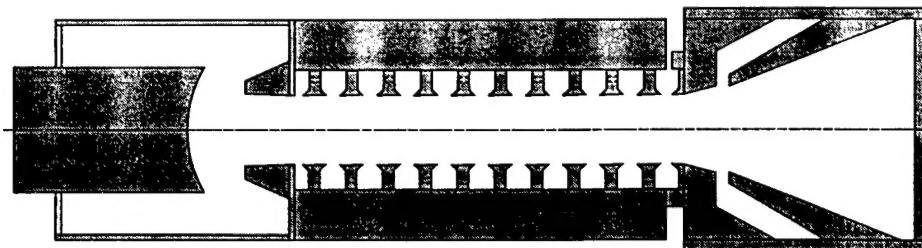


Figure 2.1: Schematic diagram of the CPI X-band TWT.

tube length was 88 cm. Smith ran the tube at $4 \times 10^{-6} < p < 1.5 \times 10^{-5}$ Torr, with typical pulse time of 1 msec. Because the background gas density was two to three orders higher than the electron density in the beam, there always existed sufficient gas for ionization in Smith's experiments. The microwave circuit was not in place – Smith was interested in measuring the ion current and associated noise. Smith collected ion current through a hole in the cathode on axis. His measurements of period versus pressure showed only a slight inverse trend.

An experimental study has been undertaken on the CCTWT by Technology Service Corporation (TSC) [11] and other contractors in cooperation with the Crane Naval Surface Warfare Center. These researchers have characterized the noise versus many parameters, as well as comparing different tubes at the same parameters. They found that some tubes exhibited no noise, while others could tune the noise on and off, while still others always had the noise signature. They noted that small changes in the magnetic field affected the noise most, followed by changes in the beam voltage and cathode filament current.

A number of theoretical studies have also been undertaken. Gilmour [2] described several possibilities for the noise, including ion buildup in the scallops followed by dumping of the ions to the cathode during a rapid collapse of the potential barrier. Lau et al. [5] proposed a mechanism for reducing the phase shift by making the interaction length an integral number of scalloping wavelengths. Manheimer [6] presented an overview of the existing models and calculated parameters including the relative importance of ionization by secondary electrons to achieve the necessary timescales, and treatment of the depressed potential as a Penning trap, in which slow electrons are trapped and ions drain to the cathode.

3. PHYSICAL MODEL

The CCTWT is shown schematically in Fig. 2.1. Electrons are emitted from a thermionic cathode at the left, and are accelerated in the anode-cathode field of 20.5 kV, traveling through the beam-circuit interaction region; the spent beam deposits the remaining energy in the depressed collector shown at the right. The parameters of operation relevant to the present study are summarized in Table 3.1.

For the background gas, it is reasonable to assume water vapor is a major constituent. Here we consider only the hydrogen component of the water vapor. Furthermore, it is convenient to take the gas density to be homogeneous, and assume full dissociation.

| parameter | value |
|---|----------------------------------|
| V | 20.5 kV |
| I | 2.86 A |
| B_0 | 0.263 T |
| mean beam radius r_b | 0.14 cm |
| anode radius r_a | 0.254 cm |
| Larmor radius r_L | 0.0136 cm |
| betatron wavelength $\lambda_b = 2\pi v_z/\omega_c$ | 1.13 cm |
| mean axial velocity \bar{v}_z | 19.8 kV = 8.34×10^7 m/s |
| beam plasma frequency ω_{pb} | 1.04×10^{10} rad/sec |
| beam cyclotron frequency ω_{cb} | 4.62×10^{10} rad/sec |
| mean beam density $n_b = I/\pi r_b^2 e v_z$ | 3.4×10^{10} cm $^{-3}$ |
| cathode temperature T_k | 0.1 eV |
| interaction length L | 19.76 cm |
| beam transit time $\tau_b = L/\bar{v}_z$ | 2.37×10^{-9} sec |
| input cavity z_{in} | 2.653 cm |
| depressed collector V_d | 13.5 kV |

Table 3.1: CCTWT parameters

4. COMPUTATIONAL MODEL

The focus of this study is to model the low frequency oscillations, and then to prescribe a method to reduce the noise. To facilitate the diagnosis procedure, a system including the electron gun and part of the drift tube was initially simulated, as shown in Fig. 4.1.

The XOOPIC code [12] is used to model the electron gun shown in Fig. 4.1. XOOPIC is a particle-in-cell (PIC) code with a Monte Carlo collision (MCC) package. It operates in either x-y or r-z geometry, and includes both electrostatic and electromagnetic field models. The MCC package is capable of handling non-reactive gas mixtures as well. Here, XOOPIC is operated in the electrostatic regime in r-z coordinates.

The program flow of a timestep for a typical PIC-MCC code is shown in Fig. 4.2. Starting at the lower right, particle charges are weighted to a mesh, to obtain $\rho(\mathbf{x})$. Poisson's equation, with appropriate boundary conditions, is then solved to obtain $\mathbf{E}(\mathbf{x}) = -\nabla\Phi(\mathbf{x})$ on the mesh. Next the fields are weighted to the continuum particle locations, and used to advance Lorentz's equations. Next, particle boundary conditions are applied. If there is a background gas, Monte Carlo collisions are then employed to obtain a modified velocity and the creation/destruction of appropriate particles. The loop then repeats with the weighting of charge to the grid.

XOOPIC presently requires boundaries comprising orthogonal segments with lengths given by integral multiples of Δr or Δz , so the cathode, anode, and focus piece are represented by stairstep boundaries. Refer to Section 5.2 for a discussion of the impact of the stairstep boundaries. The numerical parameters used in the 8 cm long models are described in Table 4.1. For the shorter models, fewer cells were generally employed in the z-direction.

| parameter | value |
|--------------------------------------|----------------------------|
| Δz | 1.25×10^{-2} cm |
| Δr | 1.2875×10^{-2} cm |
| particle weight | 2×10^6 |
| number of cells | 80×640 |
| length l | 8 cm |
| transit time $\tau_l = l/\bar{v}_z$ | 0.96 ns |
| timestep Δt | 1.25×10^{-12} sec |
| ion subcycling $\Delta t_i/\Delta t$ | 30 |

Table 4.1: Numerical parameters.

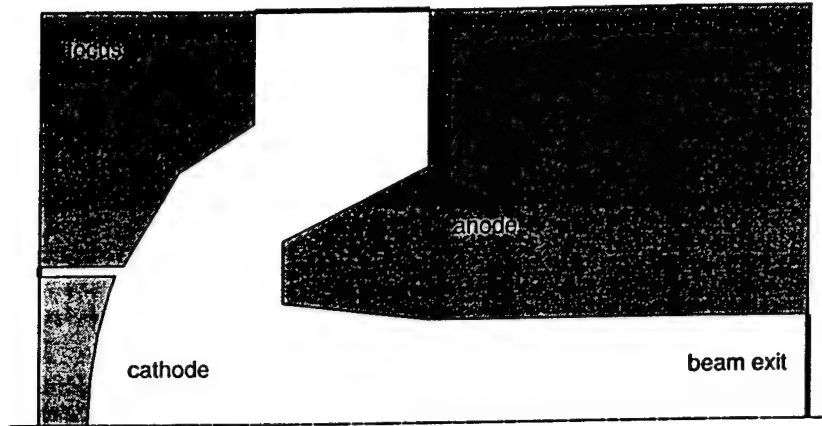


Figure 4.1: Schematic of the electron gun region, with part of the interaction region also shown.

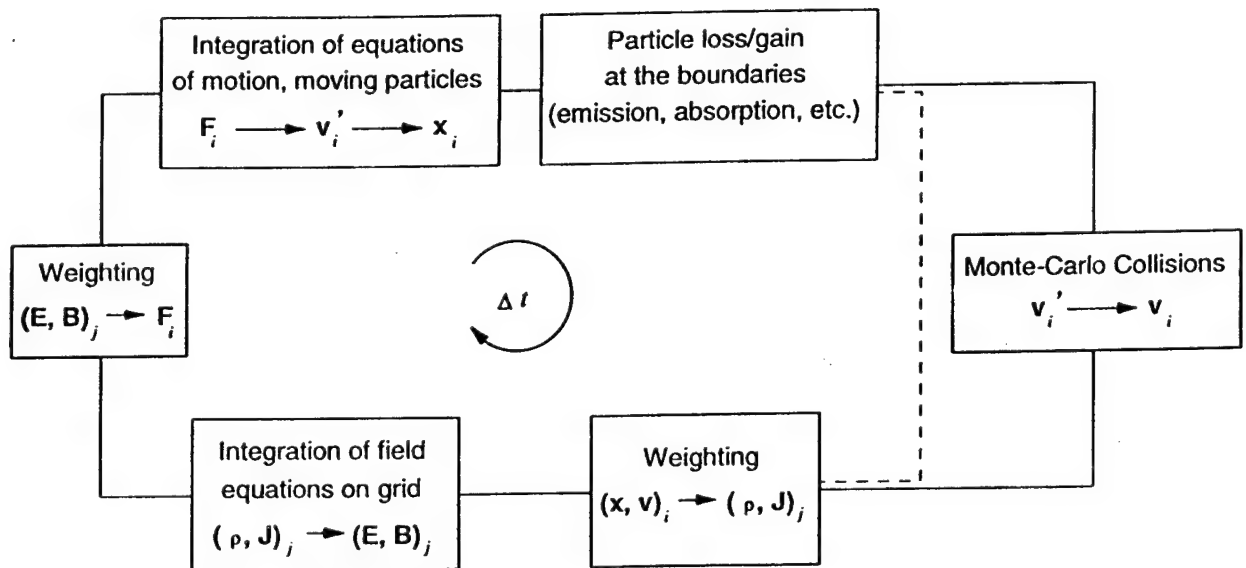


Figure 4.2: Flow chart for a timestep in the PIC-MCC scheme.

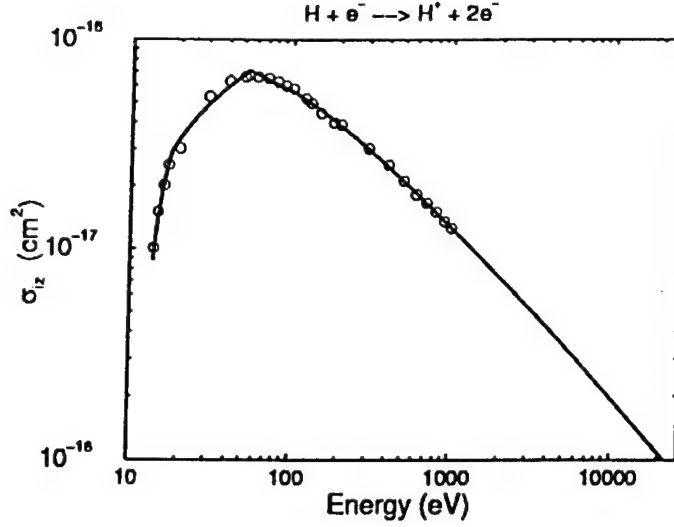


Figure 4.3: Cross section for electron impact ionization of atomic hydrogen as a function of electron kinetic energy. The symbols are experimental data points [10], and the solid line is the least squares curve fit used here.

A number of numerical parameters of interest can be computed from the physical and numerical data. An important constraint on the timestep is the electron plasma frequency; here $\omega_{pe}\Delta t = 0.013 < 0.2$, well with the regime for accuracy. Similarly, $\omega_{ce}\Delta t = 0.058 < 0.2$, also well with the tolerance for accuracy. Finally, the particle Courant condition is pushed nearly to the limit for accurate sampling of the fields, $v_z\Delta t/\Delta z = 0.834 < 1$.

The magnetic field in XOOPIC can be specified either with a data file or an equation. Here the latter is used by taking the leading terms of the solenoidal expansion (see, for example, Harman [3]):

$$B_z(r, z) \approx B_{z0} - B_{z0}'' \frac{r^2}{4} \text{ and} \quad (4.1)$$

$$B_r(r, z) \approx -B_{z0}' \frac{r}{2}, \quad (4.2)$$

where the solenoidal field on axis is given by:

$$B_{z0}(z) = \frac{B_{0,\max}}{2} \left(1 + \frac{z - z_0}{\sqrt{(z - z_0)^2 + a^2}} \right). \quad (4.3)$$

Here, $z_0 = 2.08$ cm is the axial separation of the pole piece from the cathode face, and $a = \sqrt{3}(z - z_0)_{25\%}$, where the 25% in the subscript indicates the position at which the field has dropped to 25% of the peak axial value, $B_{0,\max}$.

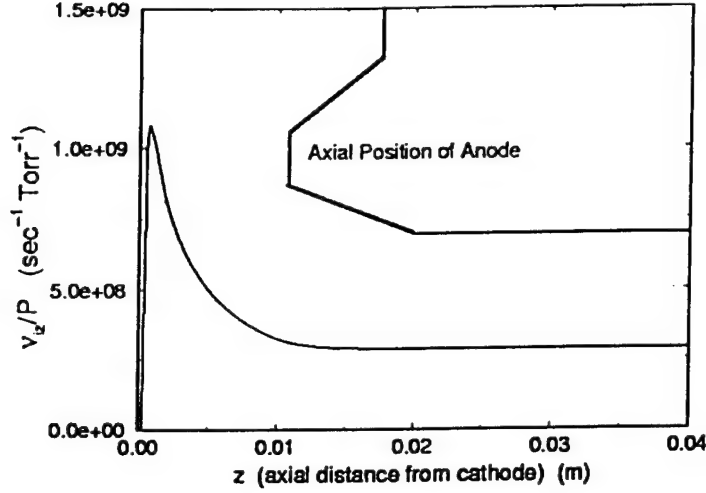


Figure 4.4: Electron-impact ionization collision frequency versus axial position for the vacuum beam.

The background gas pressure is taken as uniform and time-independent for simplicity. The gas is assumed to be fully dissociated, and volumetric recombination is neglected. The latter approximation is quite reasonable at these densities. Scattering and excitation of electrons in atomic hydrogen are neglected; the electron-impact ionization cross section used is given by (fit to data from [10]):

$$\sigma(\mathcal{E}) = \begin{cases} 0, & \mathcal{E} < 13.6 \text{ eV} \\ 8.2 \times 10^{-21} \ln(\mathcal{E}) - 2.07 \times 10^{-20} \text{ m}^2, & 13.6 < \mathcal{E} \leq 17.8 \text{ eV} \\ 3.75 \times 10^{-21} \ln(\mathcal{E}) - 7.89 \times 10^{-21} \text{ m}^2, & 17.8 < \mathcal{E} \leq 53.7 \text{ eV} \\ (3.0 \times 10^{-19} \ln(\mathcal{E}) - 8.15 \times 10^{-19})/\mathcal{E} \text{ m}^2, & 53.7 < \mathcal{E} \text{ eV} \end{cases} \quad (4.4)$$

The ionization cross section is shown in Fig. 4.3. In addition, the local ionization collision frequency is plotted versus axial position in Fig. 4.4, by taking the electron energy to be the local potential with respect to the cathode potential. Note that the ionization frequency peaks just in front of the cathode surface and decreases to a constant value as the electrons are accelerated to maximum speed. The velocity used to generate Fig. 4.4 corresponds to the vacuum potential on axis; in the presence of space charge from the beam or plasma, the collision frequency will be slightly modified due to space charge modification of the potential as well as velocity spread. These effects will be small compared to the calculation performed here.

Next we consider the importance of ion collisions, using curve fits [8] of experimental cross section data for atomic hydrogen [7]:

$$\sigma_{el} = (2.35 - 0.4 \ln \mathcal{E})^2 \times 10^{-20} \text{ m}^2 \text{ and} \quad (4.5)$$

$$\sigma_{cx} = (8.5 - 0.6 \ln \mathcal{E})^2 \times 10^{-20} \text{ m}^2. \quad (4.6)$$

The ion-neutral elastic scattering cross section, σ_{el} , for atomic hydrogen is about 10^{-19} m^2 at an ion energy of 1/40 eV, decreasing at higher energies. The ion-neutral charge exchange cross section, σ_{cx} , is about 10^{-18} m^2 at an ion energy of 1/40 eV, and also falls off with increasing energy, although more slowly than the scattering cross section. Using a maximum total cross section of $\sigma_t = 10^{-18} \text{ m}^2$, the mean free path for ion collisions is bounded by $\lambda_i = (n_g \sigma_t)^{-1} \geq 0.3 \text{ cm}$ at 10 mTorr, where n_g is the background gas density. Note that the mean free path drops an order of magnitude for ions in the 1 kV range. This indicates that ion-neutral collisions, particularly charge exchange, may play some role in moderating the impact energy of the ions accelerated into the cathode. Ions in the present model are treated as collisionless, since we are not presently interested in the ion impact energy at the cathode. If the impact energy of ions at the cathode is needed in future models, charge exchange must be considered.

A number of techniques are employed to make simulation of the broad range of timescales possible. A custom version of the multigrid elliptic solver was written to eliminate solution of Poisson's equation inside metal volumes, which comprise a significant fraction of the simulation volume, as seen in Fig. 4.1. In addition, the ions are subcycled, such that they are pushed a larger timestep than the fields and the electrons, but less frequently. Although the subcycling ratio can in principle be as large as the root of the mass ratio, $\sqrt{M/m}$, in practice the payoff is not significant above a certain level. Here a ratio of $\Delta t_i/\Delta t = 30$ is employed.

The MCC package employs the null collision method, which reduces the computation for collisions to a fraction of the full computation, given by the peak collision probability. In standard Monte Carlo methods, the energy and cross section for each individual particle must be computed each timestep. In the null collision method, the peak in collision frequency is chosen for the expected range of energy. Using the total collision frequency, the fraction of particles undergoing a collision in a timestep is a constant, P_{iz} . Next, the energy and cross sections for this subset of particles is computed, rather than the calculation for the set of all particles required in the standard method. The specific collision is then determined by computing the component collision frequencies for each type of event at the energy of the particle under consideration; the null collision event which was added to make the collision frequency energy independent indicates that a collision did not occur. For this model, the collision probability is

$$P_{iz} = 1 - \exp(-n_g \sigma_{iz} v \Delta t) = 1 - \exp(-\nu_{iz} \Delta t) \approx \nu_{iz} \Delta t, \quad (4.7)$$

where σ_{iz} and ν_{iz} are respectively the cross section and frequency for electron impact ionization, v is the electron speed, and Δt is the timestep. In the drift tube for this parameter set, we find $P_{iz} = 5 \times 10^{-4} p(\text{Torr})$, so the computation efficiency benefits of the null collision method are significant.

Another technique for improving the speed of the simulation is supercycling. In supercycling, the beam electrons are advanced more frequently than the fields, such that $\Delta t_b/\Delta t_f < 1$. This ordering of the timesteps assumes that the fields are

changing more slowly than the fast motions of the beam electrons. Unfortunately, this technique led to bunching of the beam. Further analysis demonstrated that the bunching is the manifestation of a first order term in the integration of the equations of motion which occurs when the field term is not properly time centered. It may be possible to recover second order accuracy through a more careful treatment of the fields, but for this problem the effort does not seem worth the marginal benefits in speed improvement. Supercycling was not employed in the runs described in this report.

5. SIMULATION RESULTS

5.1. Beam in Vacuum

The null collision method requires calculation of the energy and cross sections of a fraction of the number of particles given by P_{iz} , while the standard MCC method requires the calculation of these quantities for all particles.

In this section, the vacuum beam is characterized as a baseline for the following studies with background gas. The standard parameter set described above was used, with no background gas present. The simulation was run to 220 ns for the data shown here, although there is no significant change once the system has reached steady state within a few beam transit times, $\tau_l \approx 1$ ns..

The electron beam scallops as it is poorly focused in the converging magnetic field, as shown in Fig. 5.1. Note that the aspect ratio of the plot is distorted by nearly a factor of four. Because each particle in the plot represents a fixed amount of charge, uniform radial density results in a linear increase in the number of particles with radius, leading to an apparent low particle density on axis. As seen in the figure, the scalloping of the beam is not proportional to radius, and the beam forms a scalloping annulus. The space charge of the scalloping beam leads to the potential profile shown in Fig. 5.2. Note that the scale of the potential is modified to emphasize the potential wells; the cathode is at 0 V, far below the scale shown. Potential wells of about 200 V peak to peak are formed in the beam scallops due to the space charge of the beam. The radial potential depression due to the space charge of the beam is also evident, with a magnitude of about 700 V.

The velocity phase space plots provide some insight into the beam behavior. The axial velocity of all particles is shown as a function of distance from the cathode in Fig. 5.3. The beam is accelerated to about 20 kV, and the axial velocity exhibits only minor fluctuations. The radial velocity of all particles, shown in Fig. 5.4, contains a broad spectrum of velocities close to the cathode, due to the radial dependence of the accelerating field in that region. Once the beam has reached 20 kV, the radial velocity varies sinusoidally in position with a magnitude of ± 280 eV. The azimuthal velocity also varies sinusoidally with the same magnitude but 90 degrees out of phase with the radial velocity at a given axial position..

The beam exits the simulation region at the right edge. The beam energy distribution at the beam exit is shown in Fig. 5.6. The beam energy shows only a small spread. Note that a linearly increasing distribution in r indicates a uniform flux density due to the radial coordinate. From the angular distribution

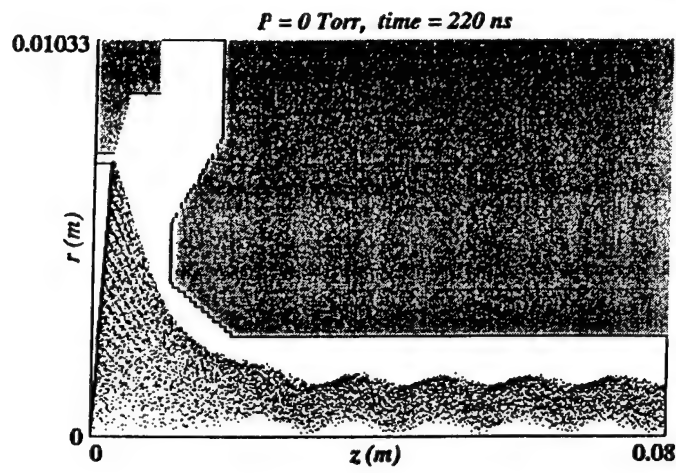


Figure 5.1: Electron beam profile in vacuum.

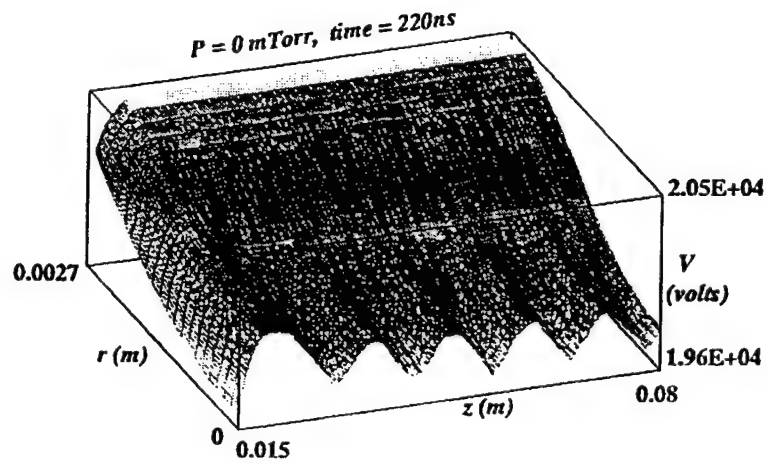


Figure 5.2: Potential as a function of position for the vacuum beam. Note that the plot is scaled to emphasize the wells formed by the scalloping beam.

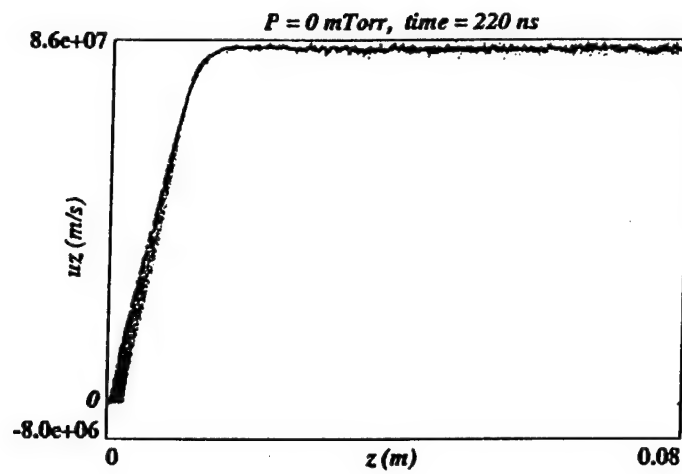


Figure 5.3: Axial velocity as a function of axial position.

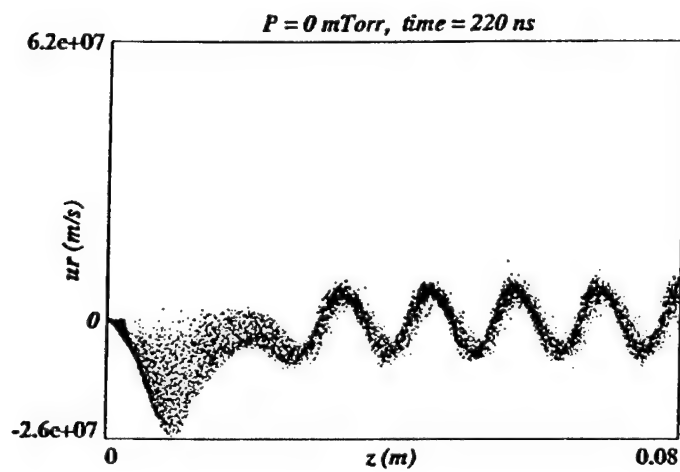


Figure 5.4: Radial velocity as a function of axial position.

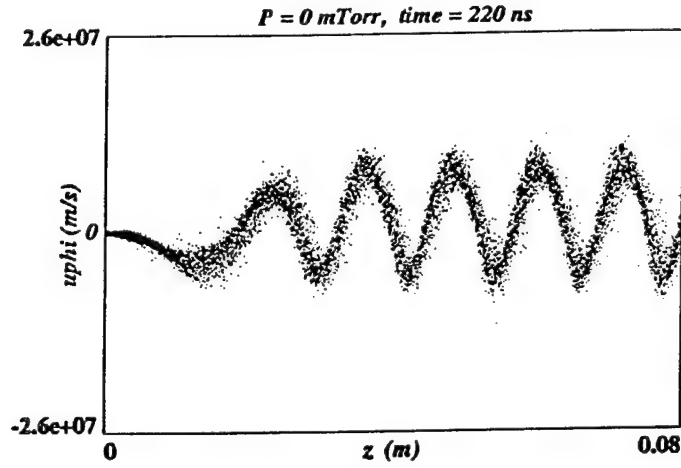


Figure 5.5: Azimuthal velocity as a function of axial position. Note that $\langle u_{\phi} \rangle = \langle v_{\phi} \rangle = \langle r\dot{\phi} \rangle > 0$, resulting in a slight net focusing of the beam.

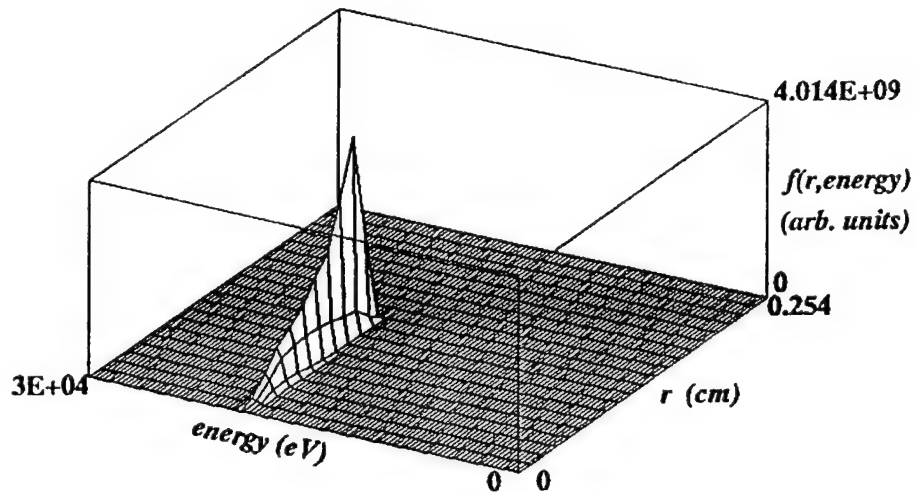


Figure 5.6: Kinetic energy distribution at the beam exit plane, $z = 8$ cm.

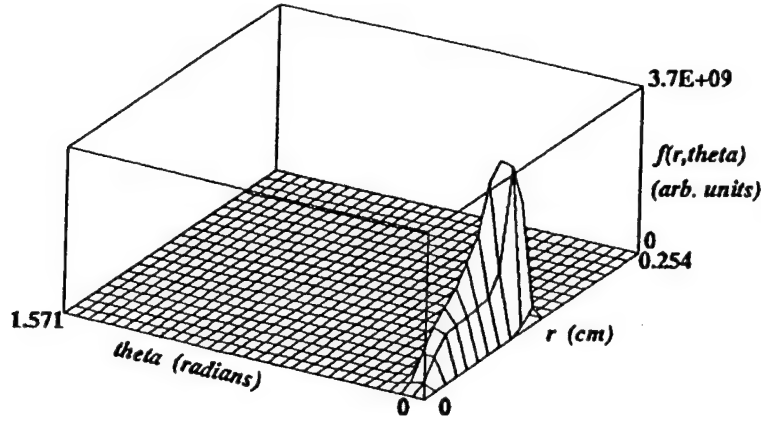


Figure 5.7: Angular distribution of particles at the beam exit plane, $z = 8$ cm.

of electrons at the beam exit, shown in Fig. 5.7, we see that the deflection angle at the beam exit is between 3 and 6 degrees.

5.2. Grid Effects

In order to ensure that the simulation is properly converged and that the effects of the striated appearance of the electron beam caused by stair-stepping of the cathode are small, several simulations were done in which the number of grids used in the simulation was varied. Three cases are discussed in this section. The number of grids used in the radial and axial directions was increased by a factor of two or four with respect to the least resolved case; see Table 5.1. The aspect ratio of the cells was held constant, so that as the number of grids was increased in the axial direction by a given factor, the number of grids was also increased in the radial direction by the same factor. Similarly, the ratio of the time step used in the simulation to the grid spacing, $\Delta t/\Delta x$, was also held constant in each case. For example, case 1, which has half as many grids in a given direction as case 2, also has a time step that is two times as large as the time step used in case 2. The particle weighting was also constant in all cases, which means that the number of particles per cell did decrease as the number of cells was increased, with implications for the noise level in potential. Note that the number of particles per cell remained sufficiently high that numerical particle heating did not play a role in this transit-time device.

The physical parameters, such as the length of the system and the current emitted by the cathode were the same in all cases. The length of the system simulated for each case in this section was 8 cm, and each case was run to a time of 7 ns. The electron transit time for this system was about 1 ns from the cathode to the beam exit. The current emitted by the cathode was 2.863 amps at a temperature corresponding to 0.1 eV.

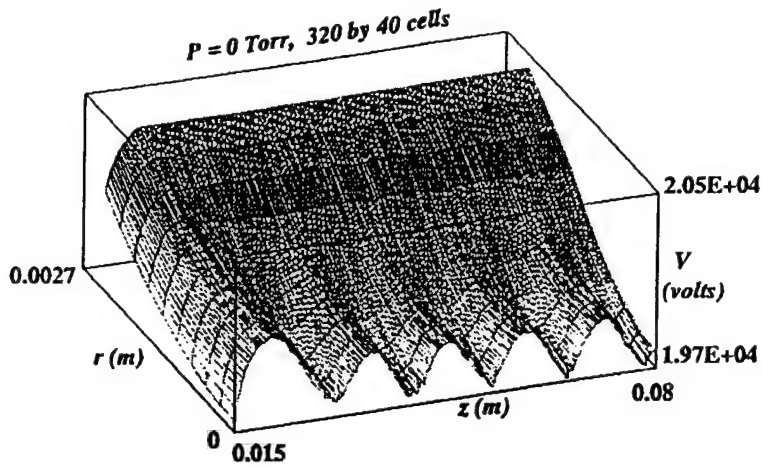


Figure 5.8: Potential within the tube region for the 320 by 40 cell grid at 7 ns.

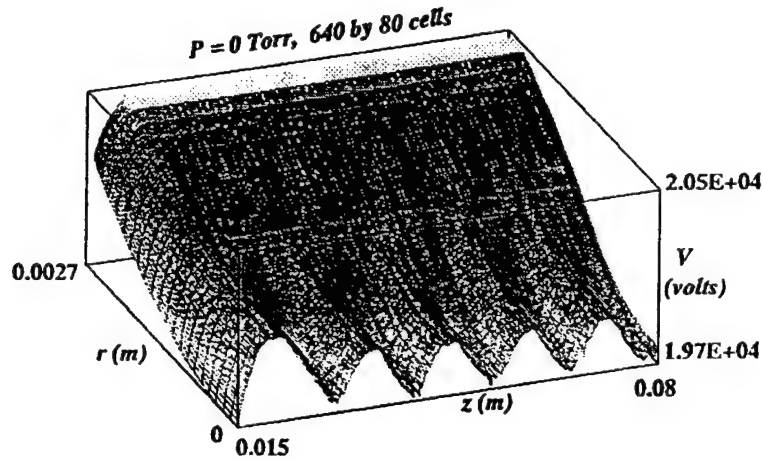


Figure 5.9: Potential within the tube region for the 640 by 80 cell grid at 7 ns.

| | cells in z | cells in r |
|--------|------------|------------|
| case 1 | 320 | 40 |
| case 2 | 640 | 80 |
| case 3 | 1280 | 160 |

Table 5.1: Resolution in the grid effects study.

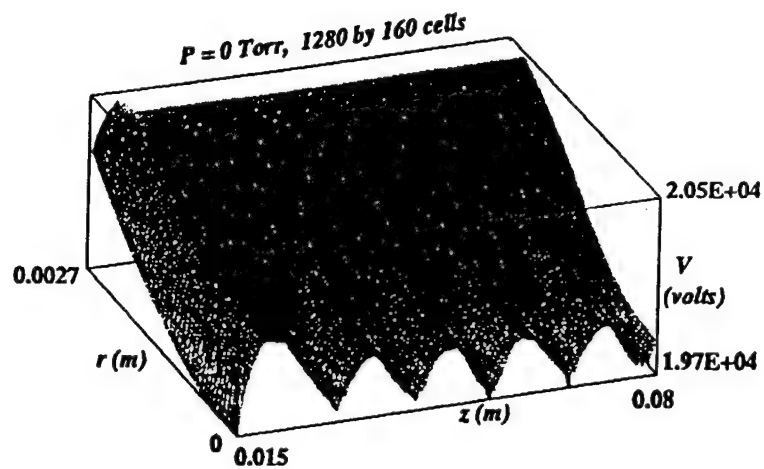


Figure 5.10: Potential within the tube region for the 1280 by 160 cell grid at 7 ns.

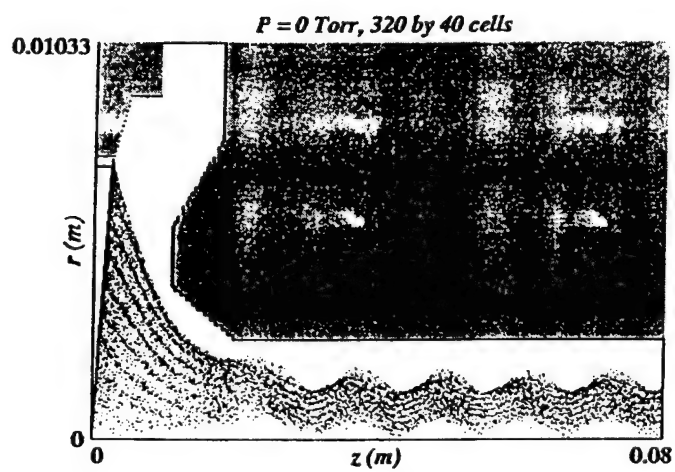


Figure 5.11: Electron position within the simulation region for the 320 by 40 cell grid at 7 ns.

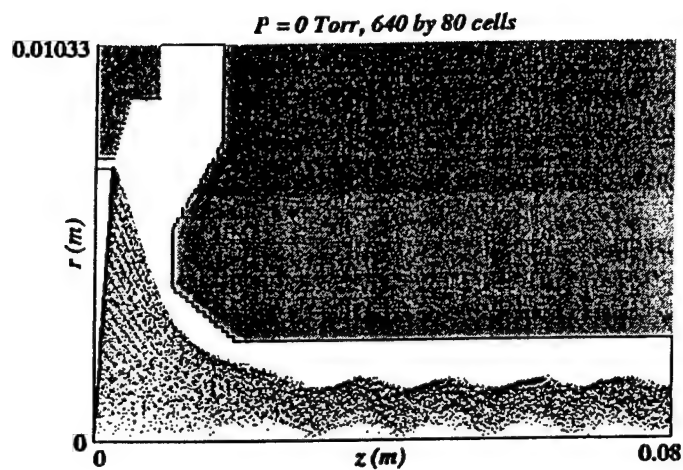


Figure 5.12: Electron position within the simulation region for the 640 by 80 cell grid at 7 ns.

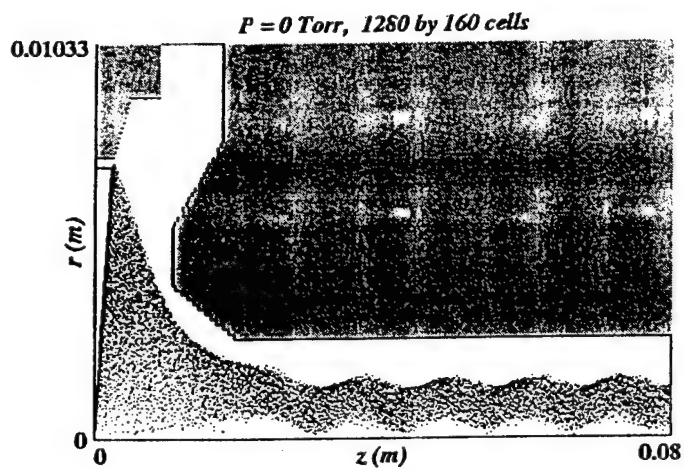


Figure 5.13: Electron position within the simulation region for the 1280 by 160 cell grid at 7 ns.

Case 1 is the least resolved case of the three and has 320 grids in the axial direction by 40 in the radial direction. Figures 5.8 and 5.11 show the potential in the drift tube region and the r-z configuration space of the beam electrons for case 1. Case 2 has 640 grids in the axial direction by 80 in the radial direction. Figs. 5.9 and 5.12 show the potential in the drift tube region and the r-z configuration space of the beam electrons for case 2. Case 3 has 1280 grids in the axial direction by 160 in the radial direction. The potential profile in the drift tube region and the r-z configuration space of the beam electrons are shown in Figs. 5.10 and 5.13 respectively.

From the potential profiles in the figures, it is clear that refining the grid has little effect on the potential. The fact that the effect of refining the grid is small is supported by the data in Table 5.2, which shows the potential differences along the beam axis ($r=0$) between the peaks and troughs in the potential for the first three ripples along the axial (z) direction. The differences in the the potential from one case to the next is, at most, on the order of 45 volts, which is quite small compared to the average potential at $r = 0$ of roughly 20 kV. Furthermore, the positions at which the peaks and troughs in the potential occur vary little between cases. It should be noted that the axial potential at $r = 0$ at a given

Table 5.2: Axial potential differences along the center of the tube ($r = 0$).

| Case number | $\Delta\phi_1$ | $\Delta\phi_2$ | $\Delta\phi_3$ | $\Delta\phi_4$ | $\Delta\phi_5$ |
|-------------|----------------|----------------|----------------|----------------|----------------|
| 1 | 312.4 | -188.0 | 228.6 | -224.5 | 241.6 |
| 2 | 341.1 | -219.0 | 251.7 | -250.4 | 237.6 |
| 3 | 349.1 | -223.9 | 230.8 | -222.6 | 245.1 |

point along z varies as much as 40 volts, or roughly 0.2 % over several time-steps due to random fluctuations, or noise, in the simulation. The particle noise from one case to the next was not a constant since the number of particles per cell was not held constant.

Figs. 5.11, 5.12 and 5.13 show the beam electron configuration space, or position within the simulated region. Some differences between the three cases are apparent in these figures. The most obvious difference is due the the stair-stepping of the cathode surface which causes the electron beam to appear to be striated into beamlets. Since the current density of the electron beam is small, $I \approx 3$ amps, the striations in the beam have little effect on the results of the simulation aside from aesthetics as was demonstrated in the discussion above.

5.3. Immobile Ion Lens

Prior to adding hydrogen to the XOOPIC model and simulating the actual ionization of a background gas, an early attempt was made to model the effects of ion

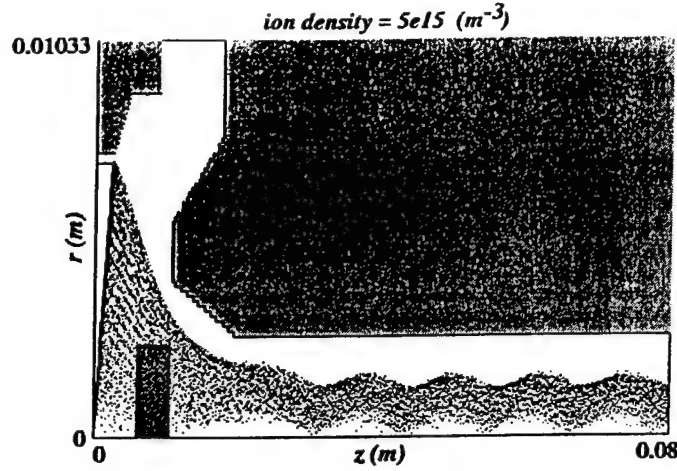


Figure 5.14: Electron positions at 8 ns with ion lens (shaded rectangle) density $n_i = 5 \times 10^{15} \text{ m}^{-3}$.

current flowing back toward the cathode from the interaction region. The presence of positively charged ions in the gun causes the electron beam to compress radially more than it would in vacuum, and may lead to extreme compression of the beam. In order to study the possibility of ion induced over focusing, a uniform density disk of immobile positively charged ions was loaded into the gun region of the simulated device.

In order to avoid initial perturbation of the electron beam at a time when no ions would be present in the device, the immobile ion disk was loaded into the electron gun region when the simulation had run for a time of 4 ns when the vacuum electron beam was in steady state. The radius of each disk was 2.5 mm and extended from 5 mm to 10 mm in the axial direction measured from the center of the cathode; therefore, the immobile ion disk was located in the region in between the cathode and anode where the electrons are not yet well confined by the magnetic field. The length of the simulated device was 8 cm, as in the previous cases discussed in this report.

Figs. 5.14 – 5.18, show the electron beam flowing through the ion lens into the drift tube for various ion number densities. The shaded region in the figures indicates the position of the ion disk. Figs. 5.19 – 5.23 are the potential profiles within the tube region of the simulation. Figs. 5.14 and 5.19 are for an ion density, $n_i = 5 \times 10^{15} \text{ m}^{-3}$, which is the lowest density shown here. Figs. 5.15 and 5.20 show the results for $n_i = 10^{16} \text{ m}^{-3}$. Figs. 5.16 and 5.21 are for $n_i = 3 \times 10^{16} \text{ m}^{-3}$, and Figs. 5.17 and 5.22 are for $n_i = 5 \times 10^{16} \text{ m}^{-3}$. The results for the highest ion density simulations, $n_i = 7 \times 10^{16} \text{ m}^{-3}$ are shown in Figs. 5.18 and 5.23.

The presence of the ion lens does causes additional over focusing of the electron beam compared to the pure electron case. The effects of the over focusing can be readily seen in the potential profiles for each case. Notice that the peaks and troughs of the axial potential profile are larger for higher ion density. Table 5.3

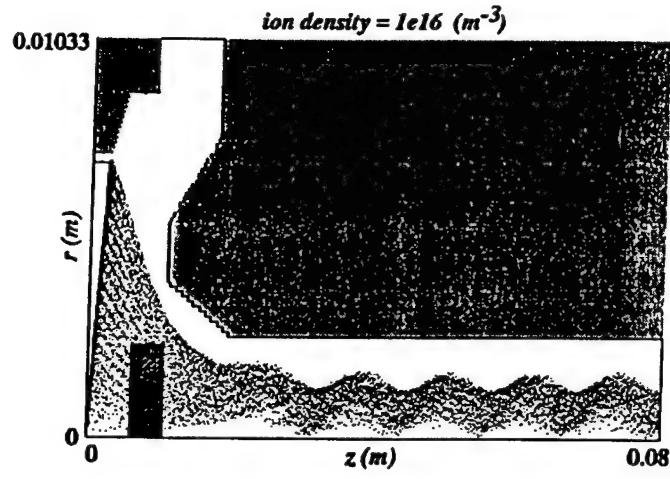


Figure 5.15: Electron positions at 8 ns with ion lens (shaded rectangle) density $n_i = 10^{16} \text{ m}^{-3}$.

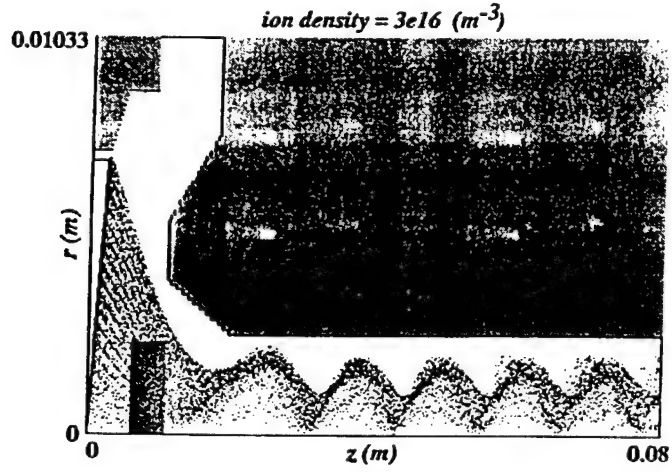


Figure 5.16: Electron positions at 8 ns with ion lens (shaded rectangle) density $n_i = 3 \times 10^{16} \text{ m}^{-3}$.

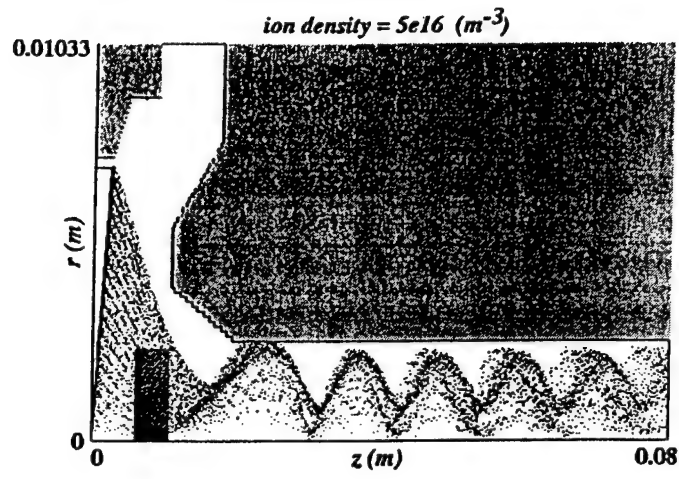


Figure 5.17: Electron positions at 8 ns with ion lens (shaded rectangle) density $n_i = 5 \times 10^{16} \text{ m}^{-3}$.

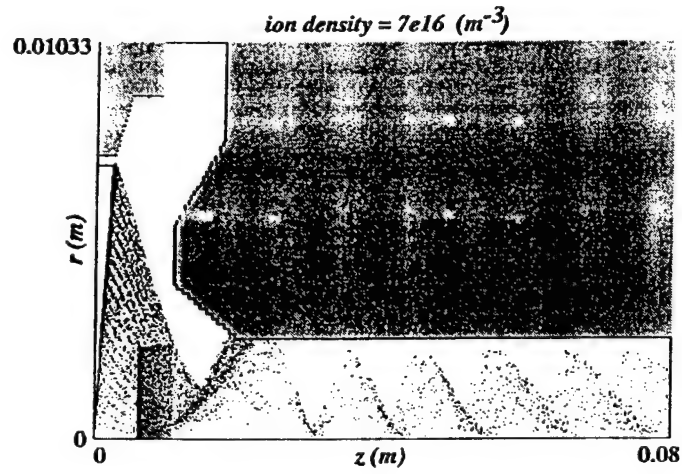


Figure 5.18: Electron positions at 8 ns with ion lens (shaded rectangle) density $n_i = 7 \times 10^{16} \text{ m}^{-3}$.

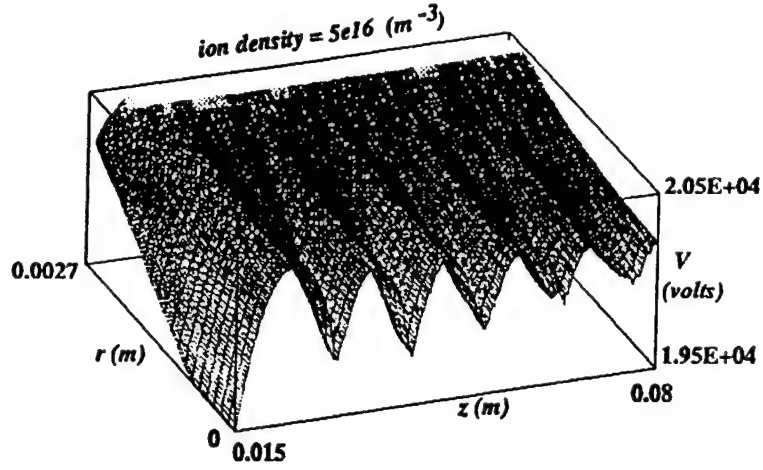


Figure 5.19: Potential profile in the tube region at 8 ns with ion lens density $n_i = 5 \times 10^{15} \text{ m}^{-3}$. Note that the voltage is scaled to emphasize the voltage in the tube region; the cathode is at 0 V.

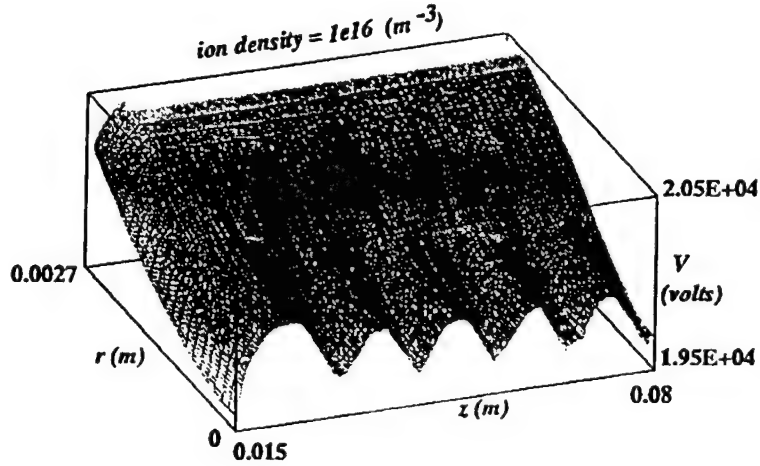


Figure 5.20: Potential profile in the tube region at 8 ns with ion lens density $n_i = 10^{16} \text{ m}^{-3}$. Note that the voltage is scaled to emphasize the voltage in the tube region; the cathode is at 0 V.

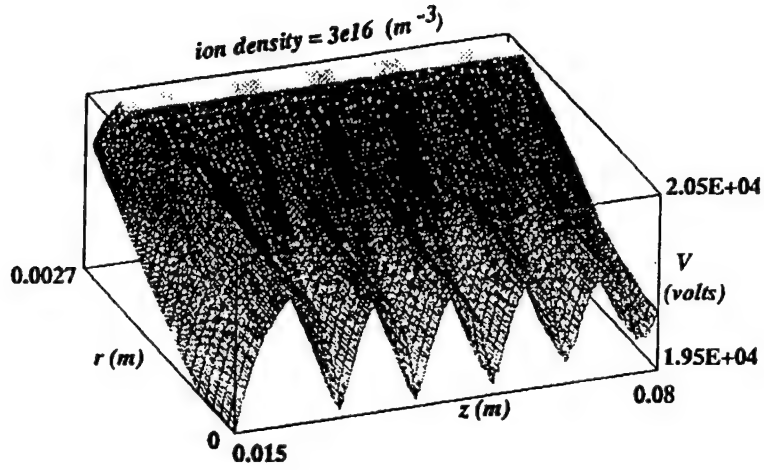


Figure 5.21: Potential profile in the tube region at 8 ns with ion lens density $n_i = 3 \times 10^{16} \text{ m}^{-3}$. Note that the voltage is scaled to emphasize the voltage in the tube region; the cathode is at 0 V.

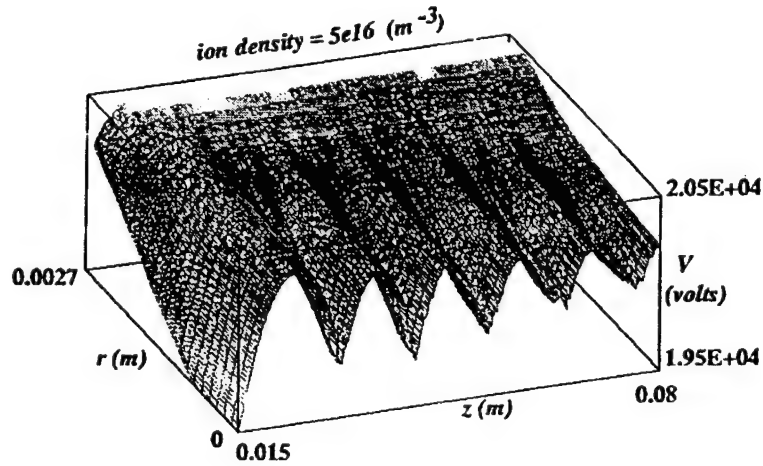


Figure 5.22: Potential profile in the tube region at 8 ns with ion lens density $n_i = 5 \times 10^{16} \text{ m}^{-3}$. Note that the voltage is scaled to emphasize the voltage in the tube region; the cathode is at 0 V.

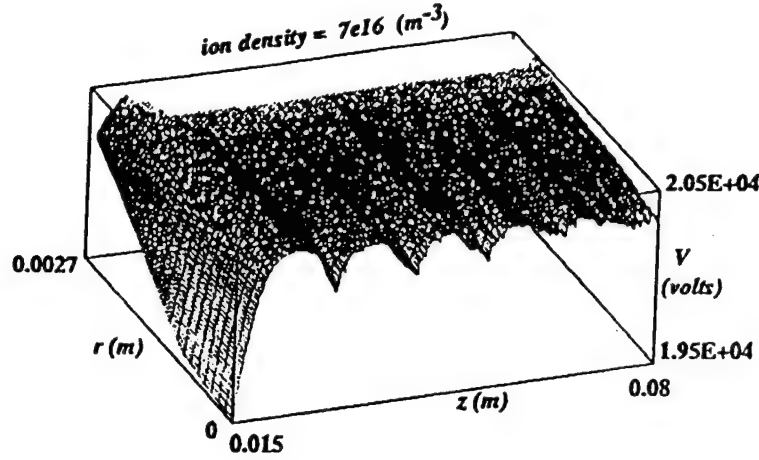


Figure 5.23: Potential profile in the tube region at 8 ns with ion lens density $n_i = 7 \times 10^{16} \text{ m}^{-3}$. Note that the voltage is scaled to emphasize the voltage in the tube region; the cathode is at 0 V.

shows the differences between the adjacent peaks and troughs in the axial potential profile along the center, $r = 0$, of the tube. As in all cases, the first potential well (peak to trough difference) is the largest, and as the beam propagates, the potential wells become roughly the same depth. However, notice the general trend

Table 5.3: Axial potential differences along the center of the tube ($r = 0$), at a time of 8 ns.

| $n_i \text{ m}^{-3}$ | $\Delta\phi_1$ | $\Delta\phi_2$ | $\Delta\phi_3$ | $\Delta\phi_4$ | $\Delta\phi_5$ |
|----------------------|----------------|----------------|----------------|----------------|----------------|
| 5×10^{15} | 318.1 | -205.8 | 251.2 | -226.8 | 190.8 |
| 1×10^{16} | 337.2 | -250.6 | 271.2 | -260.5 | 280.4 |
| 3×10^{16} | 604.5 | -514.6 | 569.3 | -557.5 | 562.1 |
| 5×10^{16} | 632.2 | -567.2 | 486.4 | -470.8 | 410.8 |
| 7×10^{16} | 243.7 | -230.7 | 186.5 | -175.6 | 140.1 |

that as the ion density increases, deeper potential wells are formed. This result is due to the fact that the beam has been radially pinched forming areas of very high density which expand out to areas of lower density creating a much larger ripple in the potential than in the vacuum case. The trend, however, does not hold true as the ion density is increased to arbitrarily large values. In both of the highest ion density cases, the beam is so extremely over focused that it intersects the wall of the tube during its expansion phase. In those cases, since more of the beam current is lost to the wall as the beam is further over focussed, the potential ripples decrease with increasing ion density, because there is not a high enough beam density remaining to depress the potential. The presence of the ion disk also shifts the position of the peaks and troughs in the potential including the

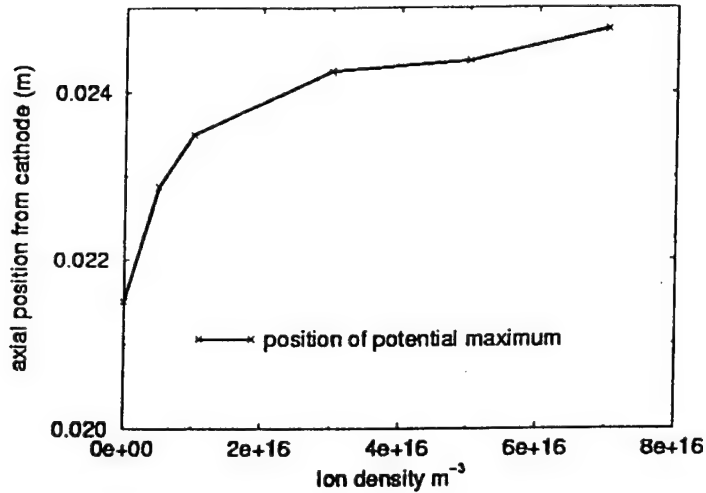


Figure 5.24: Axial location of the potential maximum as a function of ion lens density.

position where the potential is at its maximum value. Fig. 5.24 shows the axial position of the potential maximum as a function of ion lens density, where the center of the cathode is zero. The figure shows that as the ion density increases the position of the potential maximum moves farther away from the cathode, and farther into the interaction region. Both of these effects will change the amplitude of the phase noise (refer to Section A), according to Lau [5].

Figs. 5.25 and 5.26 show the contraction and expansion of the electron beam within the tube region as a function of ion density. Fig. 5.25 gives the radial extent of the beam at the first minimum in the beam radius as well as the radial extent of the beam at the maximum following that first minimum. As expected, the higher the ion density, the more the beam is contracted at the minimum, and the more it expands at the following maximum. Once again, the effect of electrons being lost to the wall is evident in the highest density case, since the maximum expansion of the beam decreases with increasing density, and the radial contraction has been magnified by a larger amount than would be expected based on the previous cases.

Fig. 5.26 shows the shift in axial position of the first radial contraction of the beam and the axial shift of the radial expansion following the first contraction. The points where the beam contracts and expands tend to shift toward the cathode as the beam is more focused by the ion disk. This information is also reflected in Fig. 5.24.

Ion densities on the order of $10^{15} - 10^{17} m^{-3}$ may be possible within the gun region for a high enough background gas pressure. However, even if such ion

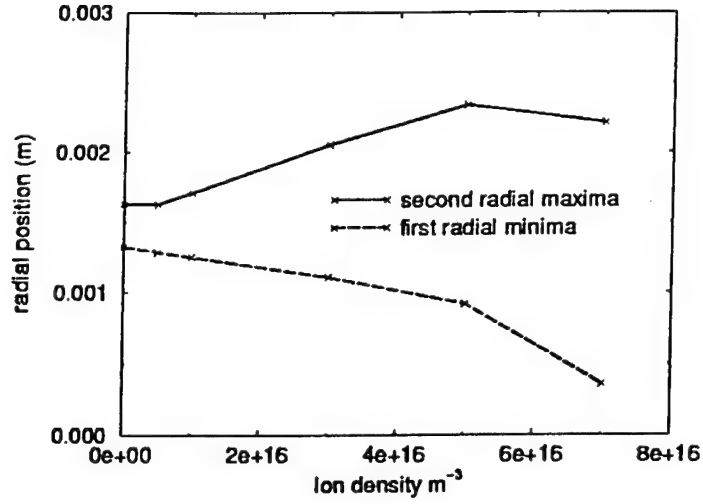


Figure 5.25: Radial location of the first minimum and following maximum in beam radius, corresponding to the maximum and minimum in potential, respectively.

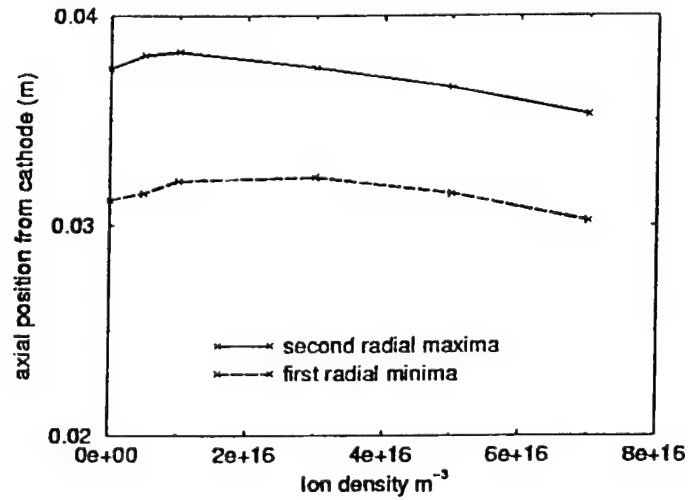


Figure 5.26: Axial location of the first minimum and following maximum in beam radius, corresponding to the maximum and minimum in potential, respectively.

densities were observed within the gun region, the simulations indicate that the ions falling back toward the cathode pinch down to a small radius and, at the axial distance of 5 mm to 10 mm from the cathode, extend to a radius of only about 0.4 mm (compared to the radius of 2.5 mm for the immobile ion disk presented here). Thus, in order to achieve the additional focus provided by the fixed ion disk modeled in this section, the densities would have to be as much as a factor of 36 higher in order to contain sufficient positive charge for equivalent focussing.

In order to make an estimate of the ion lens densities physically reasonable for the CCTWT, simple one-dimensional calculations are done as follows. In order to compare to the densities used above, the ion density within the gun region is calculated at the axial distance of $z = 0.75$ cm from the cathode. We also assume that the electrons are accelerated through an anode-cathode gap of $d = 1.5$ cm with a potential difference of $V_0 = 20.5$ kV, which implies that the axial electron velocity within the interaction region is, $v_e = 8.49 \times 10^7$ m/s. Assuming that the current densities, J_e and J_i , for the electrons flowing from the cathode into the interaction region and for the ions flowing from the interaction region toward the cathode respectively, are constant, that is, ionization within the gun has been ignored, then the following relationships be written,

$$J_e = -en_e v_e = I/\pi r_b^2 = -4.65 \times 10^5 \text{ A/m}^2 \quad (5.1)$$

where $I = 2.863$ amps is the cathode current, $r_b = 0.0014$ m is the beam radius in the drift tube, v_e is the beam velocity in the axial direction, and n_e is the electron density of the beam. From Eq. 5.1, the electron density within the interaction region is calculated to be $n_e = 3.42 \times 10^{16} \text{ m}^{-3}$. From the 10 mTorr simulations, the axial ion velocity, $v_i = -1.86 \times 10^4$ m/s (flowing toward the gun region) and the density $n_i = 9.4 \times 10^{16} \text{ m}^{-3}$ were measured at $z = 3.51$ cm. This ion velocity corresponds to an energy of 1.8 eV. Then the ion current density is $J_i = en_i v_i = -280 \text{ A/m}^2$, where the negative sign indicates that the positive ions flow in the direction opposite the electrons. Now, the ion density at the ion lens, $z = 0.75$ cm, from the cathode can be calculated to be $n_i(z = 0.75 \text{ cm}) = 1.2 \times 10^{15} \text{ m}^{-3}$, based on a potential drop for the ions of $\delta V = V(3.51 \text{ cm}) - V(0.75 \text{ cm}) = 20.5 - 8.6 \text{ kV} = 11.9 \text{ kV}$. This calculated value of ion density at the point at which the immobile ion disk was located is about one order of magnitude below the densities used in the above simulations.

Now, let us work backward, and assume that at the point, $z = 0.75$ cm from the cathode, the ion density is 3×10^{16} , which is in the midrange of the densities used in the simulations. Using the same numbers as above, that is, assuming that in the interaction region, the ions are still flowing toward the cathode at a velocity of $v_i = -1.86 \times 10^4$ m/s, and that the potential drop that the ions fall through from the interaction region to the point at which the density is measured is still 11.9 kV, then the ion current density would have to be $J_i = 7.2 \times 10^3 \text{ A/m}^2$. This means that the ion density within the interaction region would be $2.43 \times 10^{18} \text{ m}^{-3}$. This calculation is very simplistic and is not self consistent; however, both of the simple calculations indicate that the densities used in the simulations of the

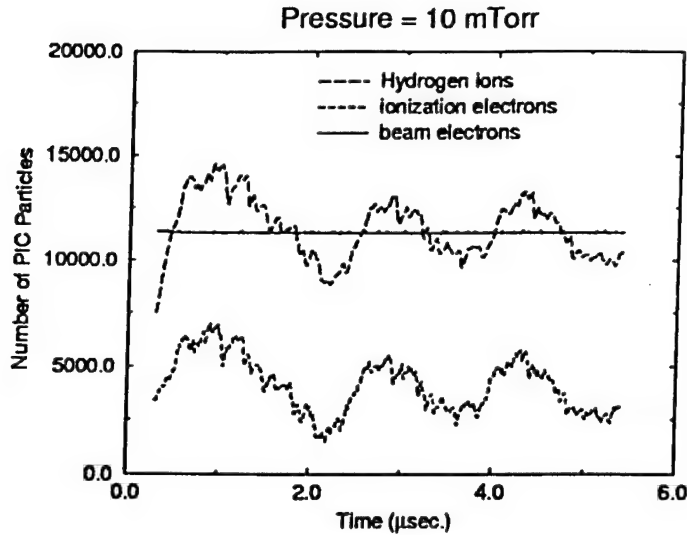


Figure 5.27: Number of computer particles at 10 mTorr.

immobile ion lens implied significantly larger ion currents than those encountered in self consistent simulations.

5.4. Self-Consistent Gun with H Gas

In this section, the details of the self-consistent PIC-MCC model with electrons, ions, and background atomic hydrogen gas are described. The configuration for the self-consistent model, shown in Fig. 4.1, is similar to the model of the preceding sections. The length of the electron gun is still 8 cm for this case.

In the self-consistent model, a background gas consisting of fully dissociated hydrogen fills the tube. The hydrogen density is taken to be uniform throughout the region of interest; in the physical device it is likely to vary considerably with distance from surfaces with the potential to outgas or getter. In this study, pressure was in the range 0.1 – 10 mTorr. The ions are modeled as collisionless, while the electrons undergo electron-impact ionization using the cross sections given in Eq. 4.4.

Electrons created in the impact ionization, called ionization electrons, are tracked separately from the beam electrons strictly for diagnostic purposes; in all physical respects the electrons are identical – the ionization electrons may also undergo electron-impact ionization collisions with the background gas.

5.4.1. Plasma Buildup

The temporal evolution of the number of beam electrons, ionization electrons, and ions is shown in Fig. 5.27 for a gas pressure of 10 mTorr. The initial buildup is

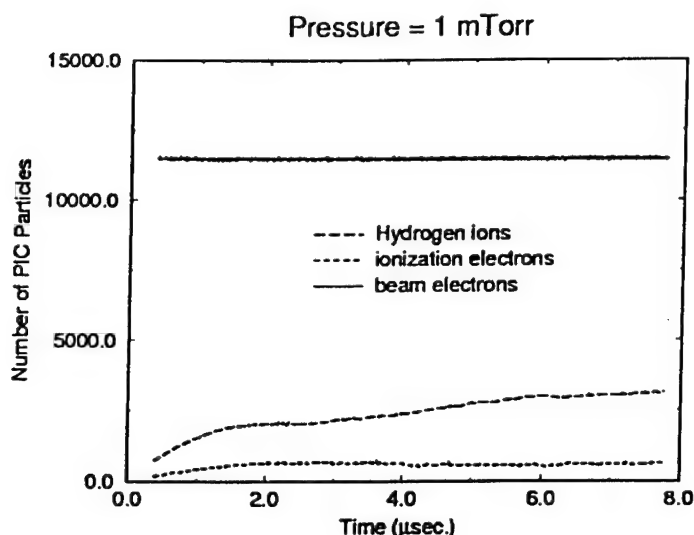


Figure 5.28: Number of computer particles at 1 mTorr.

quite rapid, with the ion density exceeding the beam density in about 250 ns. The number of ionization electrons remains significantly smaller than the number of beam electrons and the number of ions. Oscillations occur quite rapidly from the initial turn-on, within the first microsecond. The oscillations occur with a period of about $1.5 \mu\text{sec}$, corresponding to a frequency of 670 kHz, at this pressure.

The temporal evolution of the number of particles for the 1 mTorr background gas pressure case is shown in Fig. 5.28. Here we see a buildup rate for the plasma which is on the order of ten times slower, so the simulation has not run long enough to demonstrate oscillations at the lower pressure.

It is illuminating to consider the generation rate of plasma by impact ionization, in order to make an estimate for how the oscillation frequency apparent in the 10 mTorr simulation will scale with pressure. From Eq. 4.7, for long mean free paths the probability that a given electron will undergo an ionization collision in an arbitrary time interval is proportional to the background gas density, $P_{iz} = n_g \sigma_{iz} v \Delta t$. This means that the ionization rate will scale proportionally with the gas density. If we assume that the loss rate of particles is proportional to the plasma density, we find that the rate of buildup and loss and hence the oscillations will be proportional to the pressure. We can then write a simple scaling for the relationship between pressure and oscillation period to obtain the pressure for a specified oscillation period:

$$p\tau = p_0\tau_0, \quad (5.2)$$

where p_0 and τ_0 are the pressure and oscillation period from the simulation. Using $p_0 = 10^{-2}$ Torr and $\tau_0 = 1.5 \times 10^{-6}$ sec from the simulation, and $\tau = 10^{-3}$ sec for the experimentally observed oscillations, we obtain the pressure estimate

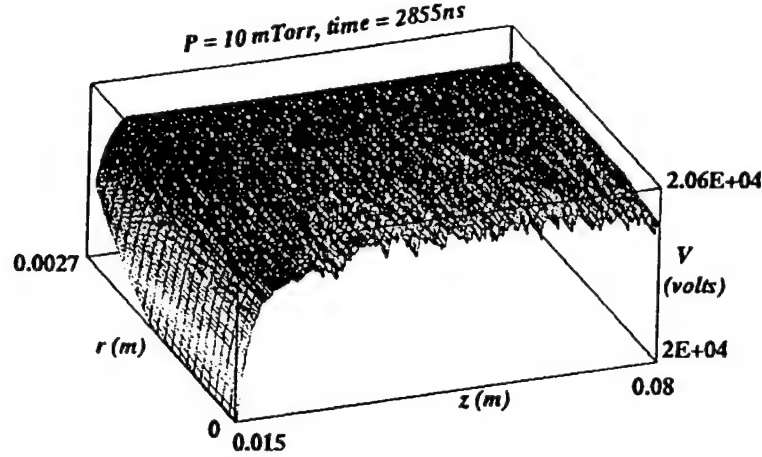


Figure 5.29: Potential in the beam line at 2.855 μsec . Note that only a narrow range of potential near 20 kV is shown; the cathode is at $V = 0$.

$p = 1.5 \times 10^{-5}$ Torr, which is a plausible pressure far from the vacuum pump.

Although the proportional scaling of the oscillation period is a good zeroeth order approximation, in reality the loss rate of a plasma depends strongly upon the electric fields, which in turn depend upon the plasma density. A self consistent nonlinear model is required for a more detailed representation of the plasma losses due to the coupling of the charge density and the fields.

As the plasma builds up, first the potential wells of the pure electron beam shown in Fig. 5.2 fill in. Next the beam potential depression also begins to fill in, and eventually, as the ion density exceeds the beam density, the potential becomes positive as shown in Fig. 5.29. The peak in the potential is about 100 V above the anode potential. The temporal evolution of the potential is also shown in Fig. 5.30; clearly the plasma raises the potential quite rapidly. It is important to note that the potential wells due to the scallops fill in when the ratio of ions to beam electrons is about 1/3, because the volume of the wells is a similar fraction of the beam volume. A similar evolution occurs on a much slower timescale for the 1 mTorr and 0.1 mTorr cases, not shown.

The location of the beam electrons is essentially unchanged by the addition of the plasma, and the vacuum configuration shown in Fig. 5.1 still applies. The location of hydrogen ions just after the peak of the number of ions, 1358 ns, is shown in Fig. 5.31. Note that the ions are most dense at the location of the beam, with significant density extending radially out toward the drift tube wall. Similarly, the number of ionization electrons at 1358 ns is shown in Fig. 5.32. The secondary electrons do not extend radially out beyond the beam radius, and are more dense downstream from the cathode. Because the avalanche mechanism will only have a noticeable impact on density over space scales of the order of the mean free path for ionization, the density disparity must be the result of axial migration of the previously trapped population.

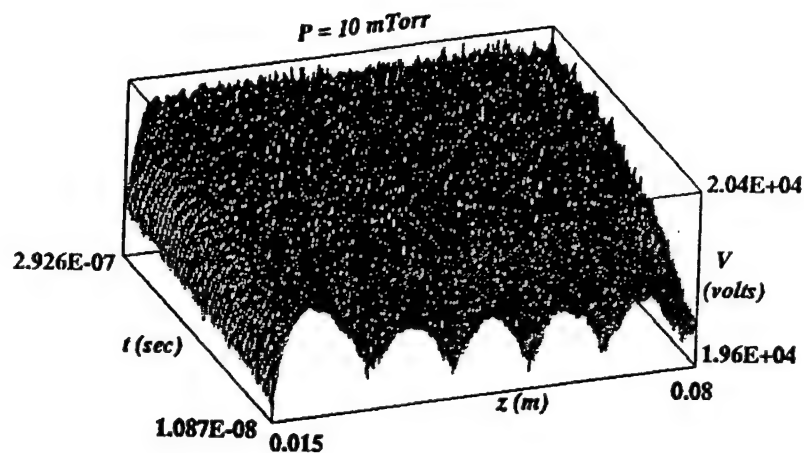


Figure 5.30: Potential along the axis as a function of time. Note that only a narrow window in potential is shown; the cathode is at zero potential.

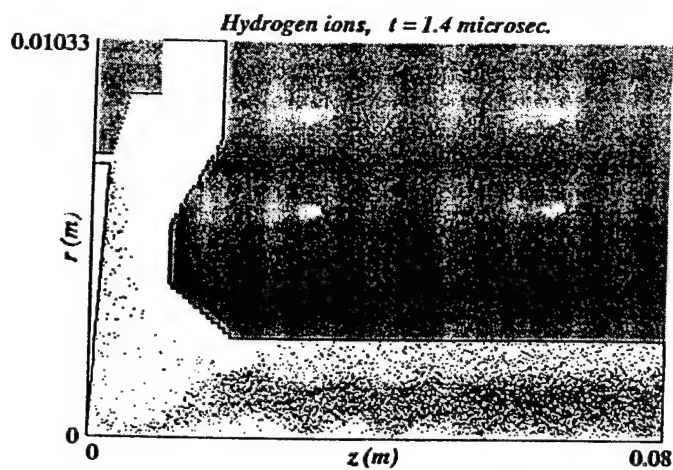


Figure 5.31: Position of hydrogen ions at 1358 ns, just beyond the maximum number of ions, at 10 mTorr.

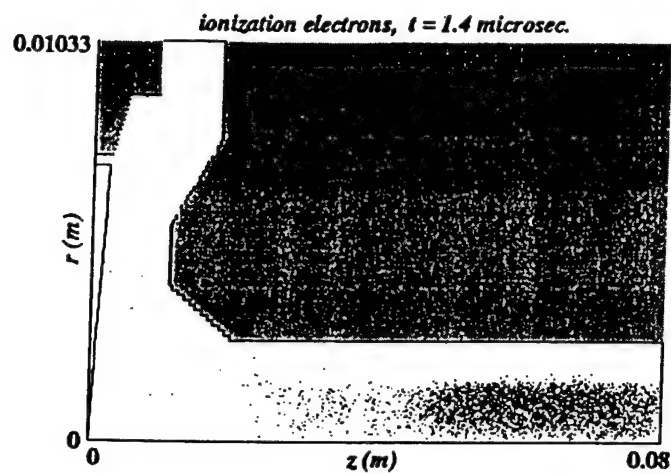


Figure 5.32: Position of ionization electrons at 1358 ns, just beyond the maximum of the number of particles, at 10 mTorr.

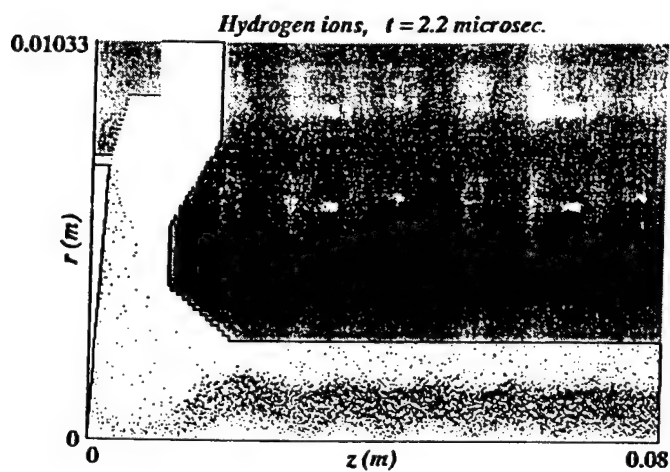


Figure 5.33: Position of hydrogen ions at 2227 ns, near the minimum in the number of ions.

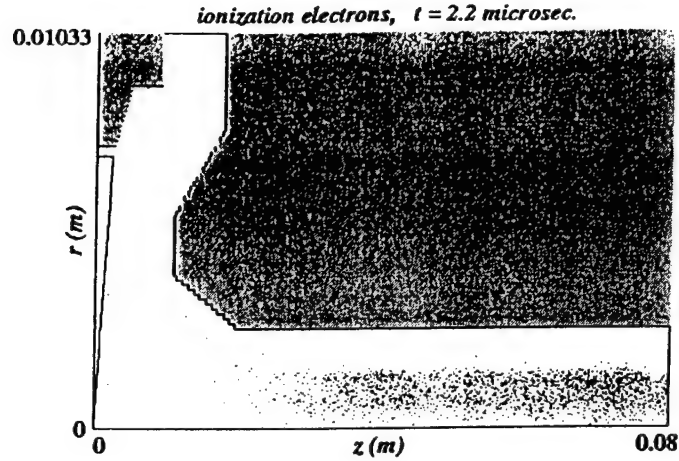


Figure 5.34: Position of secondary electrons at 2227 ns, near the minimum in the number of particles.

The location of the ions near the minimum of the number of particles, at 2227 ns, is shown in Fig. 5.33. The ions still primarily follow the beam, but the density is significantly lower, and there are fewer particles at large radii. Note that the density of particles making the excursion to the cathode is approximately the same at both the maximum and minimum of the number of particles. Fig. 5.34 shows the location of the ionization electrons at the same time, 2227 ns. The ionization electron density is more uniform axially than it was at the peak number of particles, corresponding to the upstream density at 1358 ns.

5.4.2. Exodus Mechanisms

In the previous section, the buildup of the plasma in the beamline is described. Fig. 5.27 indicates that the number of plasma particles oscillates in time. If plasma production by the beam is taken to be approximately time-independent, the loss rate must be responsible for the oscillatory nature of the plasma.

From the phase space plots shown above, Figs. 5.31-5.34, *the ionization electrons appear to be depleted axially, while the ions appear to be depleted radially.* Phase space plots of the ions and ionization electrons can illuminate the exodus process.

Next, we examine velocity phase space plots for a sequence of times, at 295, 1007, 2227, and 2855 ns. These times correspond, respectively, to the time when the potential wells are just filled, the first peak in the number of particles, the first minimum in the number of particles, and the second peak in the number of particles, as shown in Fig. 5.27.

In Fig. 5.35, the time sequence for the radial velocity components of the hydrogen ions is shown. At early times (a), as the plasma is building, the radial velocities of the ions are broadly distributed. At the peak in number (b), the radial ion velocities have cooled considerably, with a population of ions moving radially

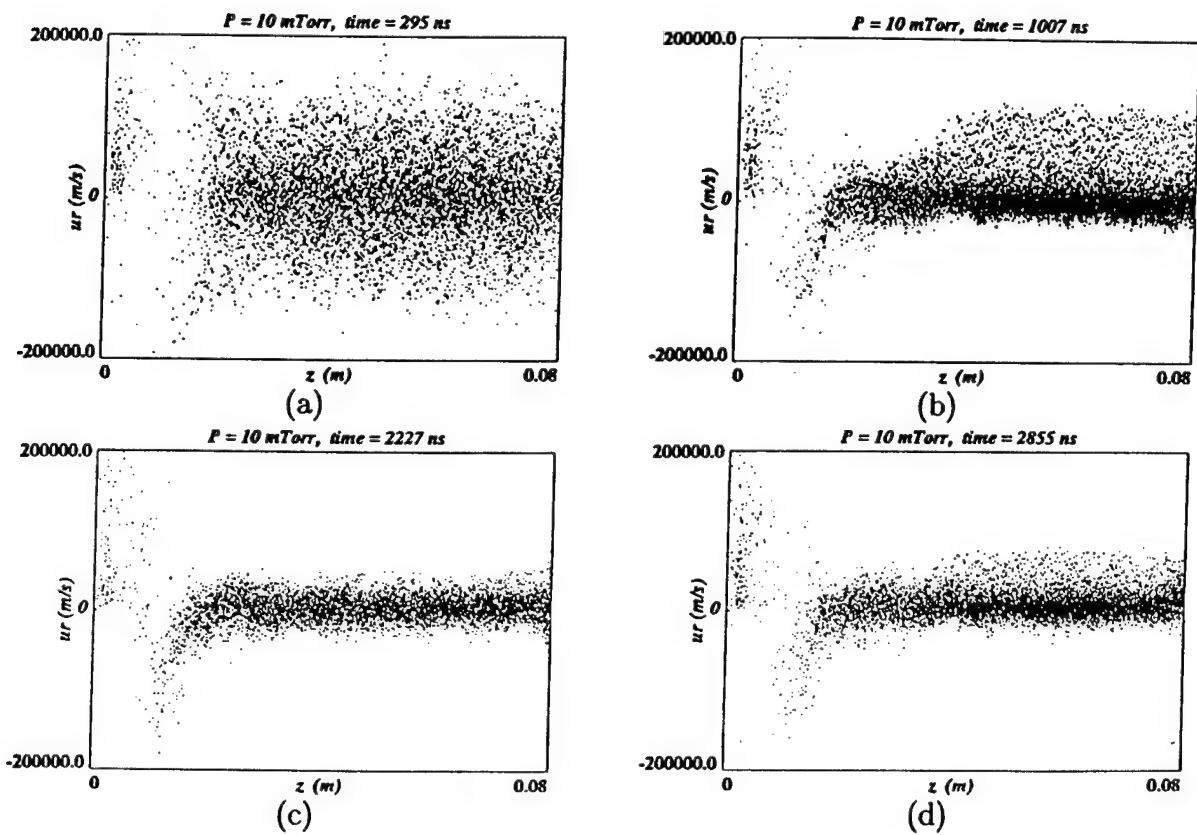


Figure 5.35: Radial velocity component of hydrogen ions for a series of times at a pressure of 10 mTorr.

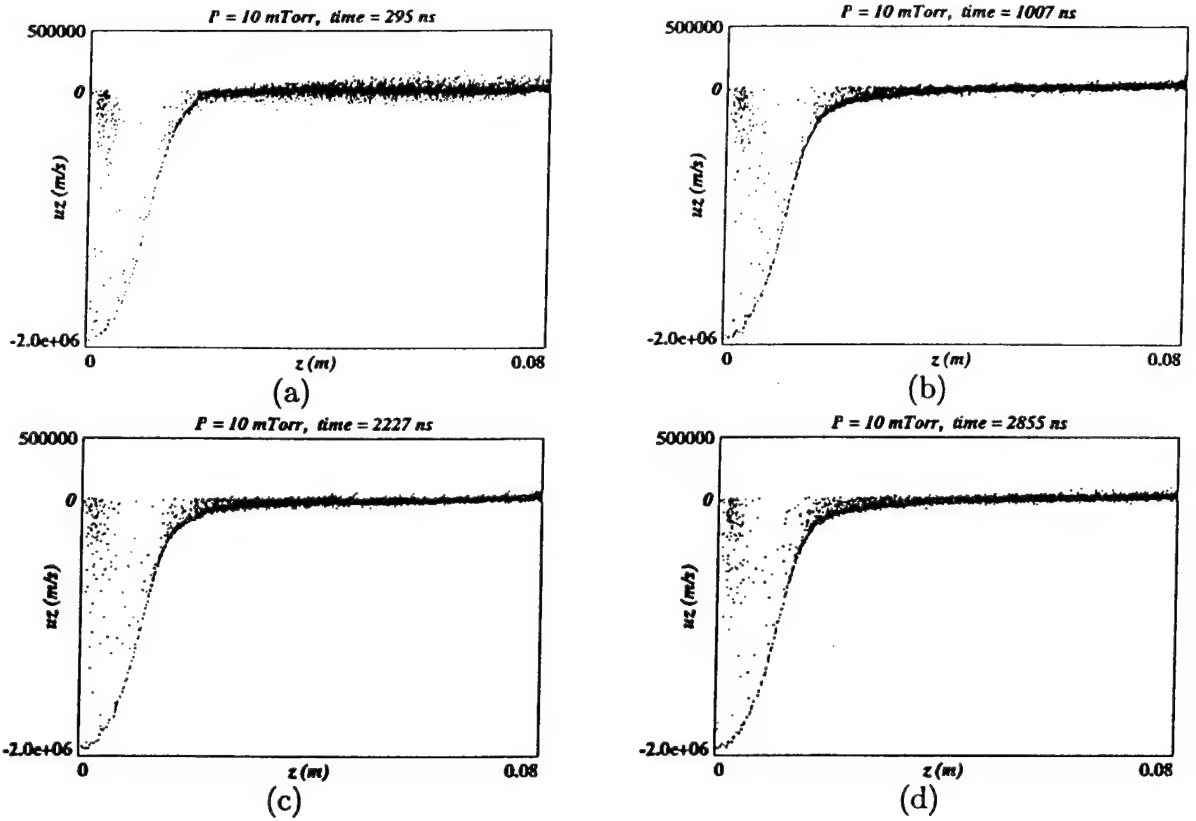


Figure 5.36: Axial velocity component of hydrogen ions for a series of times.

outward in the drift tube. At the minimum of the oscillation in the number of particles (c), the ions no longer have a significant population with outward radial velocity. Finally, at the second maximum of particle number (d), the outward radial velocity component is reforming. This sequence indicates that the ions experience a radially outward acceleration during the peak density, and cooling at the minimum in density. This is consistent with the proposed radial transport mechanism for the ions.

The axial velocity components of the hydrogen ions are plotted for the same time sequence in Fig. 5.36. Note that the velocity scale in Fig. 5.36 is much larger than that of Fig. 5.35. The axial velocity component starts out with a temperature similar to that of the radial component during the plasma buildup phase, then cools to a time-independent level during the oscillations. There is no marked change in the axial ion velocity during the oscillations. The azimuthal ion velocity, not shown, does not exhibit significant differences during the oscillation.

The radial velocity components of the ionization electrons for the time sequence are shown in Fig. 5.37. The radial velocity spread of the ionization electrons does not change much during the oscillation, but the electrons move toward the collector end during the peak of the oscillation. The azimuthal velocity components, not shown, exhibit similar behavior.

The axial velocity components of the ionization electrons are shown in Fig.

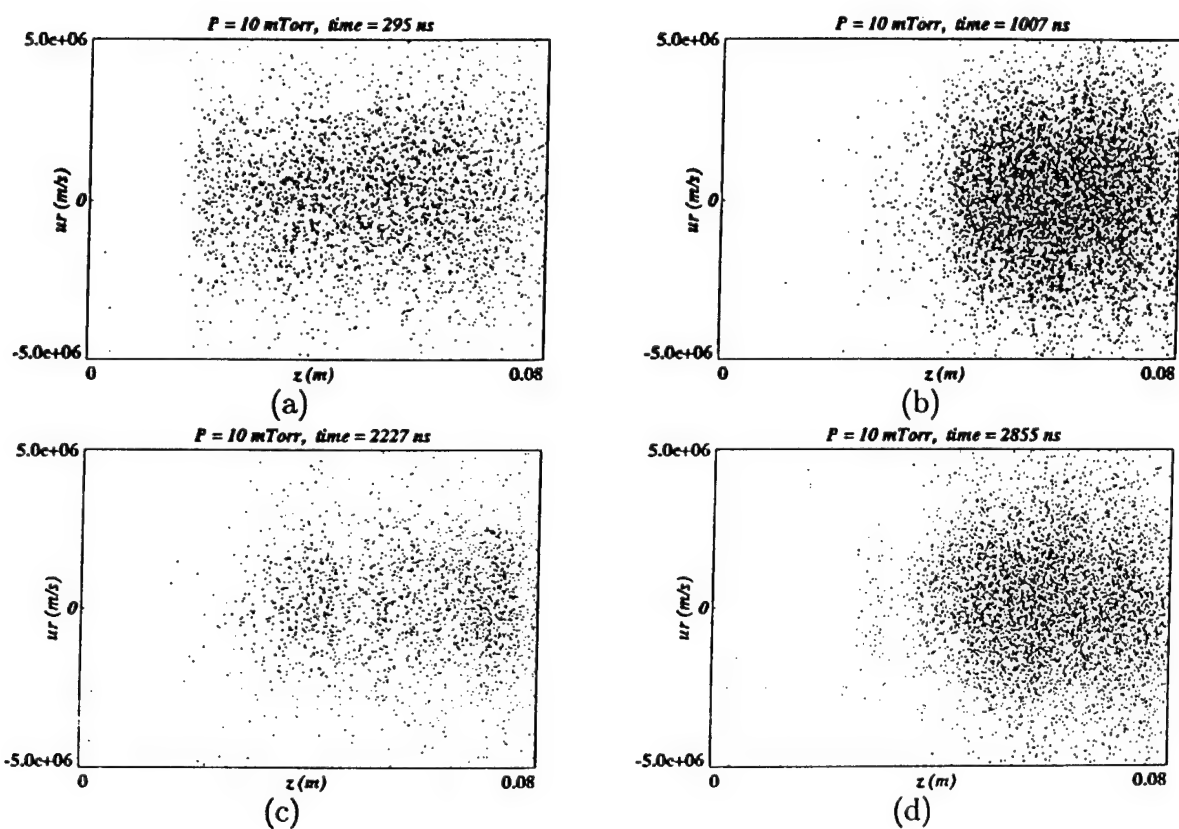


Figure 5.37: Radial velocity component of ionization electrons for a series of times, at a pressure of 10 mTorr.

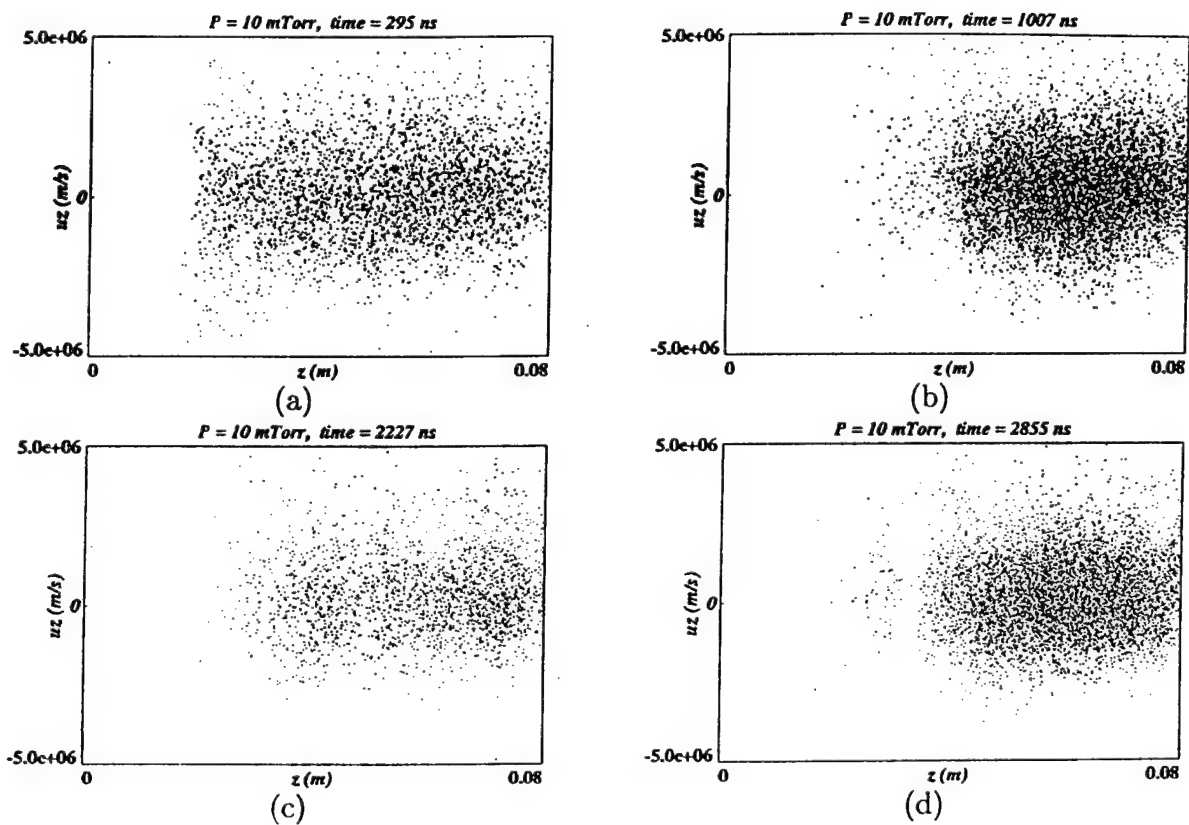


Figure 5.38: Axial velocity component of ionization electrons for a series of times, at a pressure of 10 mTorr.

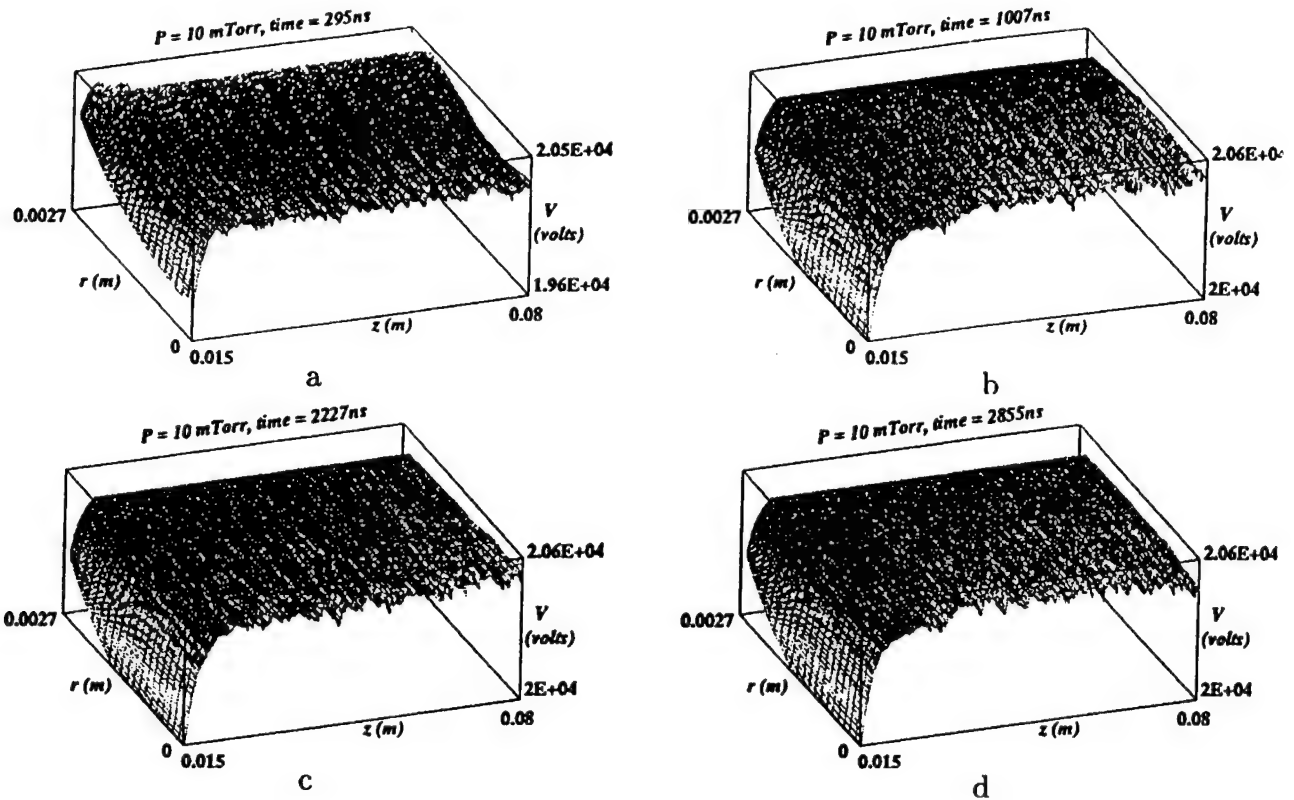


Figure 5.39: Electrostatic potential for a series of times, at a pressure of 10 mTorr. Note that the scale is magnified; the cathode is at 0 volts.

5.38. Note that the number of electrons moving in the positive direction is slightly larger than the number moving in the negative direction at all times, but this is much more evident during the peaks in the oscillation (b and d). The absence of fast electrons moving in the negative direction is partly a consequence of the non-emitting boundary condition at the beam exit, and partly a consequence of the more probable forward momentum transfer due to beam electron-impact on neutral atoms.

For completeness, the electrostatic potential is shown for the same time sequence in Fig. 5.39. During the plasma buildup (a) the beam potential depression is evident in the drift tube. At the minimum of the oscillation (c) the potential is nearly flat in the drift tube, while at the peaks of the oscillation (b and d) the potential has become positive due to $n_i > n_e$.

From the phase space and potential observed during the course of an oscillation, we see evidence supporting the radial loss of ions and axial downstream loss of ionization electrons. To determine which species is depleted first, it is useful to look at the rate of change in the number of particles in each species. From Fig. 5.40, the rate of change in the number of ionization electrons is always leading that of the hydrogen ions throughout the interval shown, over one oscillation. The same relation holds at other times as well, indicating that *the ionization electrons are expelled axially first, followed by a rise in the potential above 20.5 kV as the*

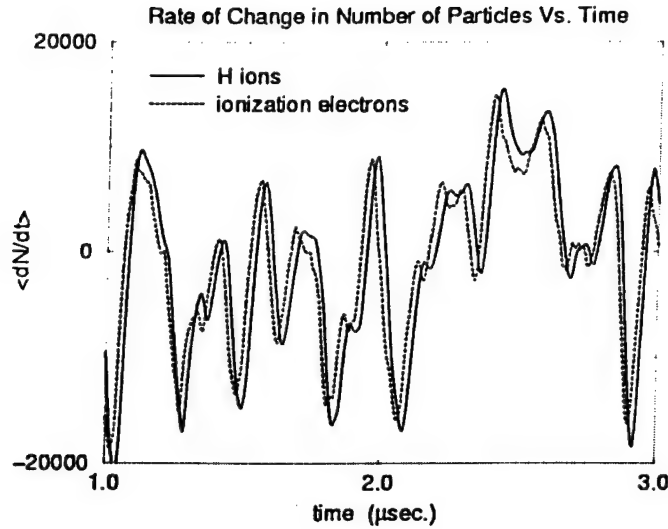


Figure 5.40: Rate of change in the number of particles versus time, at a pressure of 10 mTorr.

charge density becomes more positive, followed finally by radial expulsion of the ions 20 ns later than the electrons.

5.4.3. Phase Shift

The phase shift of the electrons with respect to the wave in the slow wave circuit is a quantity often measured by the experimentalists [11]. The phase shift for the 10 mTorr case is shown in Fig. 5.41. The derivation and calculation of the phase shift are described in Appendix A. Here we see oscillations in phase which track the oscillations previously described in the number of particles, the potential, and the various phase space quantities. By extrapolating the simulation phase shift to the full interaction length (see Appendix A), the dc phase shift is about 86 degrees, with variations of about ± 2 degrees. This compares well with experimental phase shifts of about 200 degrees with variations of ± 0.5 degrees, although the dc phase shift indicates that the beam potential, and therefore plasma density, should be somewhat higher, while the variations in those parameters should be lower. It is unclear whether any of these factors are influenced by the scaled pressure of 10 mTorr.

A similar plot of normalized phase change for a range of pressures is shown in Fig. 5.42. Note that the vacuum case is slightly off from zero phase change as a result of the difference between the integration of the potential and the drift tube velocity (see Appendix A). The phase shift is continuing to build for the lower pressure cases, and is not expected to exhibit oscillations until later in time. Indeed, the oscillations should coincide with oscillations of the number of particles.

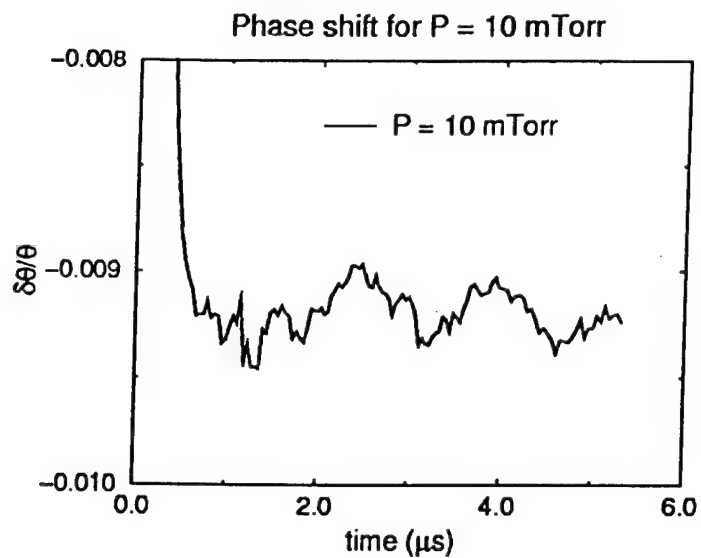


Figure 5.41: Normalized phase shift for 10 mTorr.

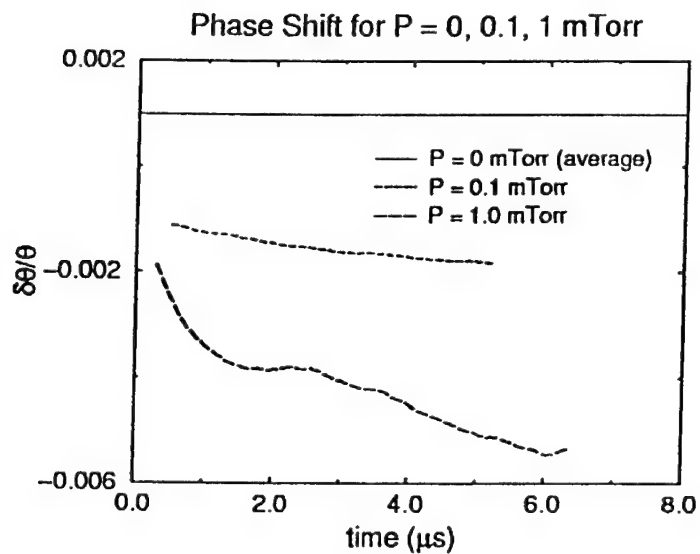


Figure 5.42: Normalized phase shifts for a range of background gas pressures.

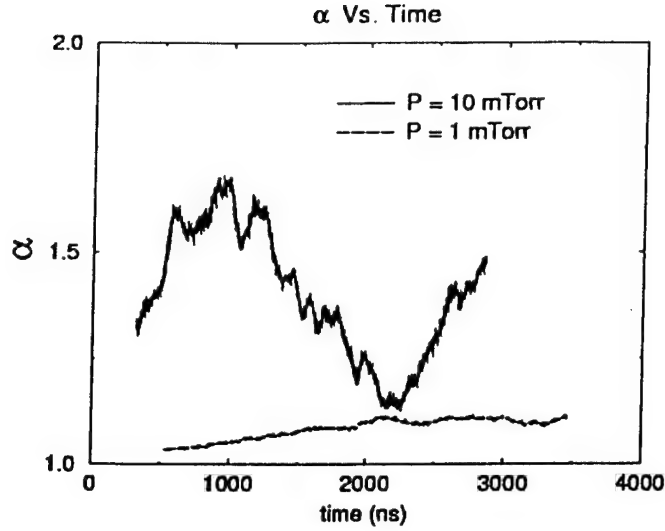


Figure 5.43: Time history of the ionization enhancement factor.

5.4.4. Ionization Enhancement Coefficient

It is interesting to consider the relative magnitude of the contribution of the ionization electrons to the ionization process of the beam. We define an ionization enhancement coefficient due to secondaries,

$$\alpha_{iz} \equiv \frac{G_b + G_i}{G_b}, \quad (5.3)$$

where G_b is the ionization rate due to the beam electrons and G_i is the ionization rate due to the ionization electrons. The ionization enhancement coefficient can be interpreted as the ratio of the total ionization rate to the rate for the beam alone. The time history of the ionization enhancement coefficient is shown in Fig. 5.43 for both the 10 mTorr and the 1 mTorr cases. Comparing Fig. 5.43 with Fig. 5.27, the enhancement coefficient profile tracks closely the total number of electrons. This means that the ionization rate per secondary electron is essentially a constant in time. Indeed, dividing the ionization enhancement factor by the total number of electrons yields a value of about 1, independent of time. *So the ionization rate of both the ionization electrons and the beam electrons are equal.*

5.4.5. Energy and Angular Distributions Exiting the Gun

The energy and angular distributions of the beam and ionization electrons were measured at the beam exit boundary, on the cathode end of the drift tube. Fig. 5.44 shows the energy distribution for the beam electrons. Note that for a radial distribution function, $f \propto r$ indicates a constant radial density. The energy distribution remains constant in time with a narrow peak at 19.7 kV, and increases

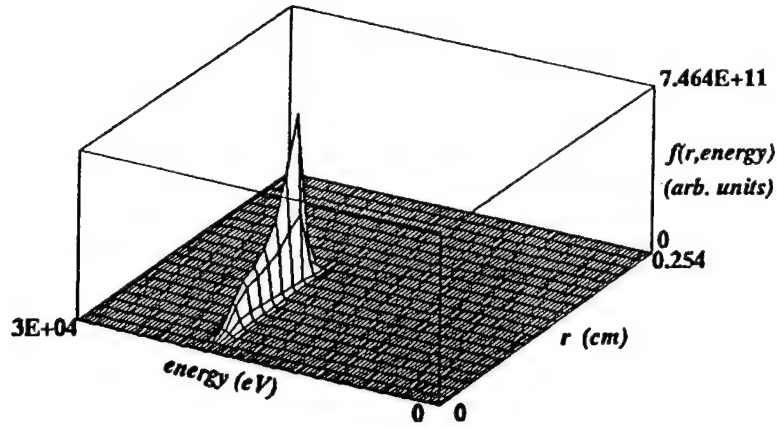


Figure 5.44: Energy distribution function of beam electrons exiting through the beam exit boundary at 295 ns for the 10 mTorr case.

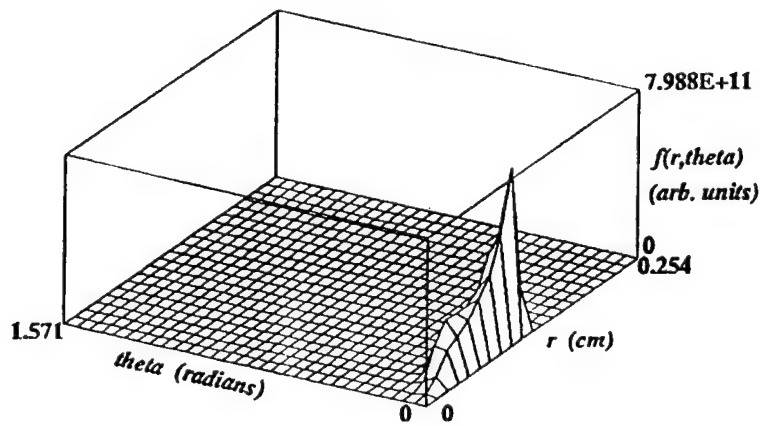


Figure 5.45: Angular distribution function of beam electrons exiting through the beam exit at 295 ns, 10 mTorr.

only slightly with pressure up to modest pressures. Similarly, the angular distribution function is shown in Fig. 5.45. The angle of the velocity is measured with respect to the normal, and includes the radial and azimuthal velocity components resulting from the gyromotion. The angular distribution is quite narrow, centered between 3-6 degrees, and is also independent of time and pressure with the ranges examined.

Shown in Fig. 5.46 are the energy and angular distributions of the ionization electrons exiting through the beam exit boundary at the plane $z = 8$ cm, sampled at a series of times. As the plasma is building up, the energy distribution (a) contains peaks at both high (nearly 20 kV) and low energies. The high energy peak corresponds to ionization events which occurred directly in front of the cathode, near the peak collision frequency (refer to Fig. 4.4). The low energy peak corresponds to plasma electrons generated in the drift tube which slowly leak out toward the collector. At 1738 ns (c), the number of particles is dropping, and the low energy peak dominates the high energy peak in the energy distribution. Because the beam is unperturbed during the oscillation, the high energy peak should be time-independent; therefore, the flux of low energy electrons is dramatically higher at this stage of the oscillation. During the upswing of the oscillation (e), the low energy peak still dominates, but comparing the low energy flux to the high energy flux, the exodus of slow electrons occurs at a slower rate. These energy distribution diagnostics provide further support for the timing of the axial exodus of ionization electrons.

The angular distribution of the velocity vector with respect to the normal of exiting ionization electrons also evolves in the temporal range described in Fig. 5.46. At 295 ns (b), the distribution is dominated by a peak at 6 degrees, with a small probability of larger angles. At 1738 ns (d), the distribution at large angles is beginning to approach the peak at 6 degrees. At 2227 ns (f), the large angle part of the distribution is again lower. The ionization electrons created near the cathode contribute only to the small angle population, which should remain independent of time. Electrons created in the drift region contribute to a broad spread of angles. Consistent with the picture of increased axial loss of slow electrons during the exodus phase of the oscillation, the large angle flux increases at 1738 ns, and subsequently decreases in the buildup phase at 2227 ns.

A similar sequence occurs at lower pressures, with an increase in the emphasis of the high energy/small angle peaks in the distributions. It is not surprising that the lower plasma density (and eventual lower generation rate in the oscillatory steady state) yields this result.

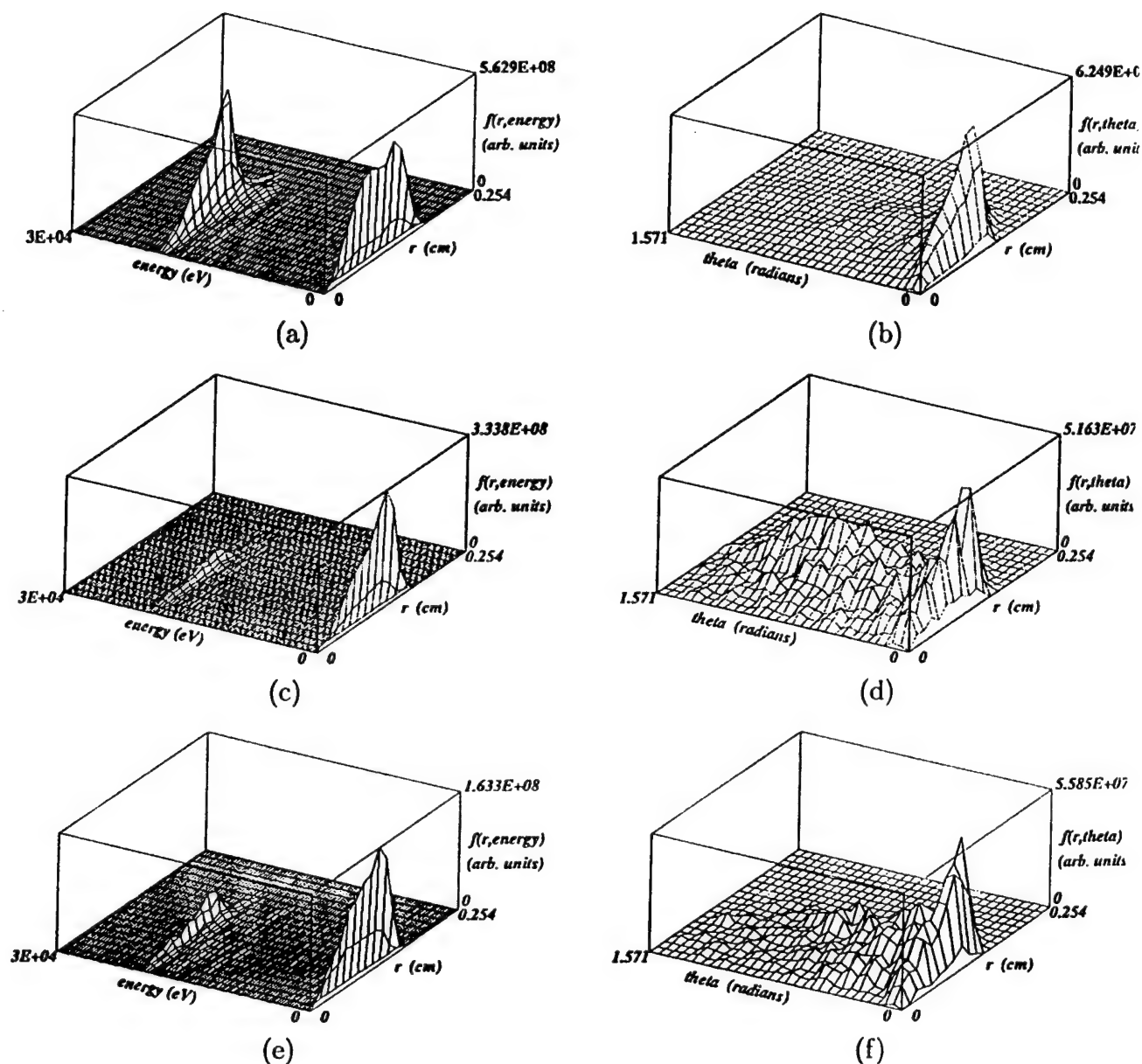


Figure 5.46: Energy distribution functions and exit angle of velocity vector with respect to the normal of ionization electrons at the beam exit for a series of times, (a,b) 295 ns, (c,d) 1738 ns, and (e,f) 2227 ns. The gas pressure was 10 mTorr.

6. CONCLUSIONS

The research performed in this reporting period included configuring the numerical model for simulation using the XOOPIC code, studying numerical grid effects, considering the impact of a plasma lens, and a self-consistent plasma model in which the gun and drift tube were filled with a background gas. Based on the information presented in this report, a number of conclusions can be drawn.

The vacuum beam study provided a baseline result, demonstrating the scalloping of the beam and the potential wells generated by the spatially oscillating beam space charge.

From the grid study presented in Section 5.2, it was shown that the grid resolution and stairstep approximation for the cathode have a very weak influence on the results of the simulation. It was found that increasing the grid resolution by a factor of four results in about a 1% change in the potential wells formed by the scalloping electron beam.

The plasma lens study also provided some useful results. First, it was shown that an ion lens formed by ions flowing in the anode-cathode gap can influence the beam profile downstream. The lens caused higher fluctuations in potential due to more extreme focusing and defocusing of the beam, and shifted the potential wells spatially. Sufficiently high ion lens density resulted in beam scrapeoff at the anode. Estimating the ion current and density required downstream in the drift tube to generate significant focusing effects, we found that ion densities one to two orders of magnitude higher than the beam density were required.

In the self-consistent plasma model, introduction of a background gas and self-consistent ionization and motion of the plasma ions and electrons were included. Low frequency oscillations were observed at 10 mTorr, and scaling these oscillations to the experimentally measured CCTWT oscillations of 0.1 - 1 kHz indicates the corresponding pressure is about 10^{-5} Torr in the gun and drift tube. As the plasma builds up, it fills in the potential wells. The ion density soon exceeds the beam density in the drift tube, leading to the oscillations as the plasma is expelled and subsequently rebuilds. The ions are observed to exit radially, while the ionization electrons exit axially towards the collector. The ionization electrons are measured to lead the ions in exodus by about 20 ns. The potential also fluctuates between positive (ion-rich space charge) at the peak in plasma density to negative (beam-depressed) at the minimum of the oscillation. The beam is weakly perturbed by the oscillation of the potential, and the result can be seen in the fluctuations of the velocity of the beam, leading to oscillations in the coupling with the circuit. The energy and angular distribution function of the beam electrons are relatively unperturbed within the pressure range studied here, always

having a narrow energy and angular profile. The energy profile of the ionization electrons leaving the simulation region are much broader, and can exhibit a double peak. In addition, the angular distribution of the exiting secondary electrons is also much broader than that of the beam electrons.

6.1. Future Work

The future work on this research includes completion of the present model, including results at lower pressures. In addition, the self-consistent model will be extended to include the collector and the diverging magnetic field in that region, expected to be important for the trapping of the slow ionization electrons which are presently discarded at the right edge of the simulation region.

In addition, the mechanism of the plasma loss must be more completely investigated, and a means of controlling the plasma oscillations must be found. Control of the plasma oscillations are believed to be the key to control of the noise in the CCTWT.

A two-dimensional parametric circuit model is planned to connect to the PIC beam, allowing significantly improved run times over a multi-cavity electromagnetic PIC model. This model will use a Kirchhoff-Maxwell boundary condition to interface the circuit to the PIC region, allowing study of the circuit interaction with the modulated kinetic beam. Finally, a self-consistent three-dimensional electromagnetic PIC model is proposed to provide a baseline comparison to the simplified model.

7. ACKNOWLEDGMENTS

This work was supported by Office of Naval Research contract number N00173-98-1-6001. The work has benefitted from significant collaboration with personnel from the Naval Research Laboratory (B. Levush, W. M. Manheimer, M. A. Kodis, B. Danly) as well as with W. James at CPI and Y. Y. Lau at the University of Michigan.

A. PHASE CALCULATION

In this appendix, the change in phase is calculated in two slightly different ways, and a comparison is made. First, the phase is calculated using the definitions for the phase shift, $\delta\theta$ or $\Delta\phi$, used by Y.Y. Lau and W. Manheimer respectively. Next, the phase shift is calculated simply by taking the difference between the total phase for a given system at a specific time and the total phase calculated from the simulation for a pure electron case. The phase shift in the body of this report is calculated using the second method presented in this appendix.

From Manheimer [6], it is noted that a simple dispersion relation for a traveling wave tube amplifier may be written as

$$(\omega - kv)(\omega - kv_{ph}) = -\alpha^2, \quad (\text{A.1})$$

where ω is the rf signal frequency, v_{ph} is the phase velocity in the slow wave circuit, k is the wave number, v is the axial velocity of the beam electrons, and α is the coupling coefficient. Solving Eq. A.1 for the wave number yields,

$$k = \frac{(v + v_{ph})\omega \pm \sqrt{\omega^2(v - v_{ph})^2 - 4vv_{ph}\alpha^2}}{2vv_{ph}}. \quad (\text{A.2})$$

The phase length, θ , is simply the integral of the real part of the wave number over the axial distance, z , from the input cavity to the output cavity,

$$\theta = \int_0^L \frac{(v(z) + v_{ph})\omega}{2v(z)v_{ph}} dz. \quad (\text{A.3})$$

The maximum amplification occurs when the beam velocity is equal to the phase velocity, $v = v_{ph}$. Thus, for maximum amplification, the total phase length, is $\theta = \omega L/v$, where L is the total interaction length. Relaxing the constraints somewhat, and allowing for slight variations in the beam velocity, the total phase length may be written,

$$\theta = \int_0^L \frac{\omega dz}{v}, \quad (\text{A.4})$$

as presented by Lau et al. [5]. As noted in Lau's paper, changes in the electron velocity δv , will lead to shifts in the phase,

$$\delta\theta = - \int_0^L \frac{\omega \delta v}{2v^2} dz, \quad (\text{A.5})$$

where $\delta\theta$ is the phase shift. (The factor of two in the denominator of Eq. A.5 was missing in Lau's paper, but was noted by Manheimer [6]. It is a consequence

of the fact that the phase velocity of the rf signal does not change, whereas the velocity of the beam does fluctuate; see Eq. A.2.)

For the purpose of this report, it is assumed that the beam electrons, of charge e , and mass m , are moving at a velocity in the axial direction resulting from acceleration through a potential drop of V_0 , the potential difference between the anode and cathode corrected for the potential depression of the space charge of the beam, thus,

$$v \approx \sqrt{\frac{2eV_0}{m}}. \quad (\text{A.6})$$

Substituting this expression for velocity into Eq. A.4 and integrating yields,

$$\theta = \sqrt{\frac{m}{2e}} \frac{\omega L}{V_0^{1/2}}. \quad (\text{A.7})$$

Similarly, Eq. A.5 can be written as,

$$\delta\theta = -\sqrt{\frac{m}{8e}} \int_0^L \frac{\omega \delta V}{2V_0 V(z)^{1/2}} dz, \quad (\text{A.8})$$

where $\delta V = V(z) - V_0$, and $V(z)$ is the potential along the axis, $r = 0$, of the tube as a function of z , the distance along the interaction region. If the potential, $V(z)$ is known at discrete points, $V_j \equiv V(z_j)$, Eq. A.8 can be numerically integrated,

$$\delta\theta \approx -\frac{1}{2}\omega\sqrt{\frac{m}{8e}} \sum_j \frac{\Delta z}{2V_0} \left(\frac{\delta V_j}{V_j^{1/2}} + \frac{\delta V_{j+1}}{V_{j+1}^{1/2}} \right), \quad (\text{A.9})$$

where $\Delta z \equiv z_{j+1} - z_j$. Dividing Eq. A.9 by Eq. A.7 gives the expression,

$$\frac{\delta\theta}{\theta} \approx -\frac{\Delta z}{8LV_0^{1/2}} \sum_j \left(\frac{\delta V_j}{V_j^{1/2}} + \frac{\delta V_{j+1}}{V_{j+1}^{1/2}} \right). \quad (\text{A.10})$$

In order to evaluate the data from the simulations and compare to experimental results, it was necessary to make a few approximations and assumptions. We assume that the mean beam velocity in the z (axial) direction within the interaction region is equal to the phase velocity for the vacuum case. The axial velocity was measured from the simulation to be approximately 8.34×10^7 m/s at the beam exit, which corresponds to an accelerating potential difference of roughly $V_0 = 19,700$ volts. The simulations do not extend to the length of the actual traveling wave tube, thus, a truncated interaction length was used in the calculations. The interaction length, L , was measured from the point corresponding to the middle of the input cavity to the end of the simulated system, rather than to the middle of the output cavity. In comparing to experiment, it is assumed here that the ratio of the change in the phase to the total phase length is roughly constant throughout the interaction region. That is, in order to compare to the phase change measured in experiment, $\delta\theta/\theta$ measured from simulation is multiplied by the total phase length corresponding to the full interaction length from the input to output cavities.

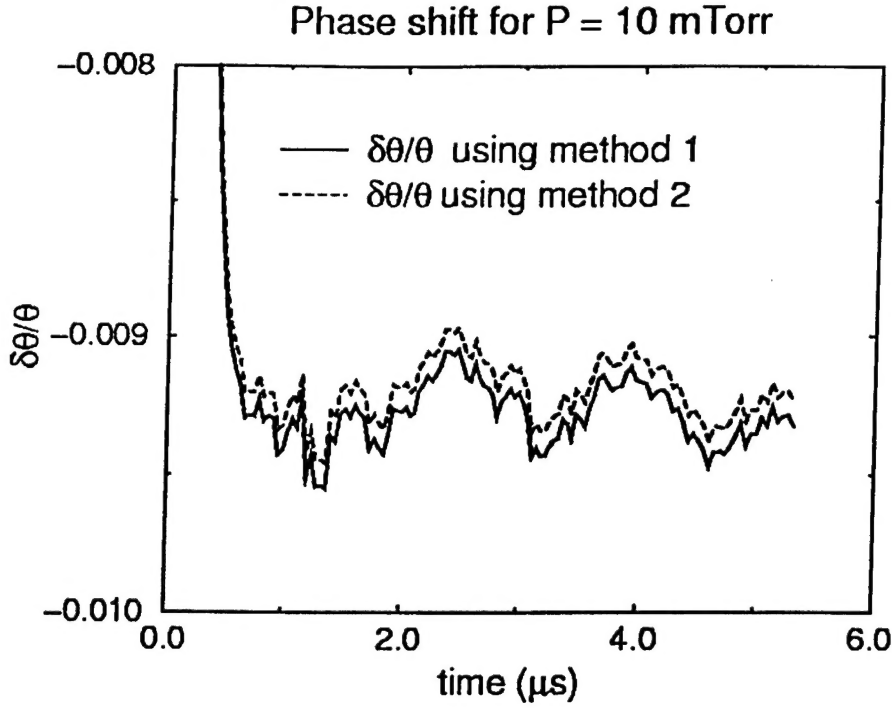


Figure A.1: Phase shift comparison at 10 mTorr calculated using the two methods described in this Appendix. Method 1 is described in [5] and [6]; Method 2 is the alternative method described in the second part of this Appendix.

As an example, let us consider the results of the phase shift for the 10 mTorr gas pressure case. Since the simulations were done using a total length of 8 cm, then the interaction length used in the calculations is 5.35 cm. The unperturbed beam velocity and phase velocity of the wave are assumed to be equal and have a value of $v \approx 8.34 \times 10^7$ m/s. The signal frequency, ω , is taken to be 11 GHz, a value in the mid-range of X-band. From these values we find that $\theta_s \approx 2,540$ deg, which corresponds to a phase length for the actual twt of $\theta \approx 9,380$ deg. The velocity fluctuations in the beam are calculated assuming that the beam velocity follows the potential profile on axis. In other words, $\delta v(z) = \sqrt{e/2m\delta V(z)}/V(z)^{1/2}$, where $\delta V(z) = V(z) - V_0$, and $V(z)$ is the axial potential within the interaction region at the time that the phase change is measured. The value of $\delta\theta/\theta$ calculated for the 10 mTorr pressure case fluctuates about a value of ~ -0.0094 , corresponding to a 1% change in the phase. Note that in this case, the potential on axis was raised by about 3.5% and the beam velocity increased by about 1.7%.

The phase shift could have alternatively been defined as the total phase length measured in the system at a given time minus the total phase length measured in the pure electron case, which is our base case. Referring back to Eq. A.3, we may write the total phase length at any time as the integral of the real part of the

wave number over the interaction length, where it is not assumed that the beam velocity is equal to the phase velocity nor constant over the interaction region,

$$\theta_i = \int_0^L \frac{(v_i(z) + v_{ph})\omega}{2v_i(z)v_{ph}} dz, \quad (\text{A.11})$$

where θ_i is the total phase length at some time, $t = t_i$, and $v_i(z)$ is the beam velocity as a function of distance from the input cavity at time, $t = t_i$. The phase shift at $t = t_i$ is then just defined as,

$$\delta\theta_i = \int_0^L \frac{(v_i(z) + v_{ph})\omega}{2v_i(z)v_{ph}} dz - \theta, \quad (\text{A.12})$$

where $\theta = \omega L/v$ is the total phase length when the beam velocity is equal to the phase velocity, $v = v_{ph}$. Eq. A.12 can be simplified to,

$$\delta\theta_i = \sqrt{\frac{m}{2e}} \int_0^L \frac{\omega}{2\sqrt{V_i(z)}} dz - \frac{\theta}{2}, \quad (\text{A.13})$$

where Eq. A.6 has been used, and $V_i(z)$ is the axial potential along $r = 0$ at time $t = t_i$. Figure A.1 shows the phase shifts calculated using Eq. A.8 (method 1) and using Eq. A.13 (method 2). As seen in the Figure, there is a very small shift between the two the values, the second method showing a slightly smaller shift in the phase (the vacuum phase shift for a beam without scallops being near zero). The text, Section 5.4.3, employs method 2.

BIBLIOGRAPHY

- [1] L. D. Clough, K. Evans, H. L. Hartnagel, and P. C. Kendall. Low frequency output fluctuations of microwave tubes. *International Journal of Electronics*, 27:195, 1969.
- [2] S. Gilmour. Some comments concerning ion noise effects in the CWI TWT. unpublished, 1998.
- [3] W. W. Harman. *Fundamentals of Electron Motion*. McGraw-Hill Book Company, Inc., 1953.
- [4] H. Klostermann and A. Rodhe A. Piel. Ion sheath oscillations around a strongly negative grid in a DP-machine. *Bulletin of the American Physical Society*, 41, 1996.
- [5] Y. Y. Lau, D. Chernin, and W. Manheimer. A note on noise in linear beam microwave tubes. *submitted to IEEE Trans. Electron Devices*, 1998.
- [6] W. M. Manheimer. On the theory of ion noise in microwave tubes. Technical Report NRL/MR/6707-99-8323, Naval Research Laboratory, 1999.
- [7] E. W. McDaniel. *Collision Phenomena in Ionized Gases*. John Wiley & Sons, New York, N.Y., 1964.
- [8] H. B. Smith. *Computational Studies of an Asymmetric rf Plasma using Particle-in-cell Techniques*. PhD thesis, Australian National University, 1994.
- [9] J. K. Smith. *Ion Drainage in High Power Klystrons*. PhD thesis, Cambridge University, 1972.
- [10] H. Tawara, T. Kato, and M. Ohnishi. Ionization cross sections of atoms and ions by electron impact. Technical Report IPPJ-AM-37, Institute of Plasma Physics, Nagoya University, Nagoya, Japan, 1985.
- [11] D. Thelan and S. MacMullen. private communication. selected results presented at the Low Frequency Noise Workshop, New Orleans, LA, 1998.
- [12] J. P. Verboncoeur, A. B. Langdon, and N. T. Gladd. An object-oriented electromagnetic PIC code. *Comp. Phys. Comm.*, 87:199–211, 1995.